Influence of Rapid Intramolecular Motion on NMR Cross-Relaxation Rates. A Molecular Dynamics Study of Antamanide in Solution

R. Brüschweiler,[†] B. Roux,[‡] M. Blackledge,[†] C. Griesinger,[†] M. Karplus,*[,‡] and R. R. Ernst*[,†]

Contribution from Laboratorium für Physikalische Chemie, Eidgenössische Technische Hochschule, 8092 Zürich, Switzerland, and Department of Chemistry, Harvard University, Cambridge, Massachusetts 02138. *Received July 1, 1991*

Abstract: An 800 ps molecular dynamics simulation of antamanide in chloroform has been used to study the influence of fast angular and radial intramolecular dynamics on experimentally accessible homonuclear NMR cross-relaxation rates. Correlation functions of the intramolecular motions, needed to compute the cross-relaxation rate constants, are derived from the molecular dynamics simulation. The spatial restriction of the relative motion of two nuclei involved in the cross relaxation is described by an angular and a radial order parameter in a molecule-fixed reference frame. It is found that the generally opposite effects of angular and radial motion on cross-relaxation rates are separable to a good approximation. The applicability of the separation is discussed for some analytical motional models. When internal motional processes and the overall rotational tumbling are taking place on a similar time scale as the inverse Larmor frequency, systematic differences between NOESY and ROESY cross-relaxation rates are predicted from the molecular dynamics simulation and interpreted in terms of order parameters and internal correlation times. Possibilities for extracting information on internal motion by combining experimental NOE and ROE cross-relaxation data are discussed.

1. Introduction

The widespread use of multidimensional NMR methods for the elucidation of biomolecular structure in solution is based on the interproton distance information contained in NMR cross-relaxation rates[1,2] and provided by NOESY-type experiments.[3-6] Such distance information, often supplemented by measured scalar coupling constants,[7,8] can be used for the determination of the structure of molecules in this normal medium;[9,10] i.e. solution structures are obtained rather than the structures in a crystal that are determined by X-ray methods. Experimental cross-relaxation rates can be directly related to interproton distances only in the absence of internal motion. For biomolecules under physiological conditions, atomic fluctuations and side chain motions are important,[11] and their effect on the cross-relaxation processes[12] can be significant.

The potential of NMR relaxation studies to characterize internal motion was recognized many years ago[13] and the extensive work in this field over the last 3 decades was recently surveyed by Kowalewski.[14] The experimental approach makes use of analytical motional models to fit the relaxation data. The models normally describe restricted internal motion by either diffusive or discrete lattice jump processes or by combinations of the two.[15,16] Although parameterized analytic dynamic models provide a detailed description of the motional properties, they may tend to overinterpret the experimental information. Since the number of model parameters often is as large as the number of observable quantities, it is difficult to determine whether the model itself is valid.

Another source of valuable information concerning the type of possible motions and the feasibility of specific models is molecular dynamics simulations.[11] An example is provided by the computed carbon-13 nuclear magnetic relaxation rates obtained from stochastic dynamic simulations of alkanes and aliphatic amino acid side chains.[17] Calculated and experimental relaxation rates were compared and used to check the validity of various analytical models for the internal motions.

An alternative, so-called model-free approach, circumvents overinterpretation of experimental data by the description of the internal dynamics by generalized order parameters and correlation times of spin pairs. Experimental data have been interpreted in this manner by Lipari and Szabo.[15] Olejniczak, Dobson, Karplus, and Levy[12] extended this study to proton NMR in lysozyme. They estimated the relative contributions of angular and radial motions to the order parameter by use of a molecular dynamics simulation in vacuum. In a study of short-time correlation functions and NMR relaxation of liquid acetonitrite, Westlund and Lynden-Bell[18] separated distance and angular terms of the intermolecular dipolar correlation function and showed that they are approximately statistically independent. Farmer et al.[19] examined the influence of anisotropic global motion on NOESY and ROESY cross relaxation in the presence and in the absence of internal motion about one axis. Analogous molecular dynamics studies of motional effects on other NMR parameters, such as vicinal coupling constants[20] and ring-current-induced chemical shifts[21] have also been made where the effect of distance and angular

* Corresponding authors.
† Eidgenössische Technische Hochschule.
‡ Harvard University.

(1) Solomon, I. *Phys. Rev.* **1955**, *99*, 559.
(2) Noggle, J. H.; Schirmer, R. E. *The Nuclear Overhauser Effect, Chemical Applications*; Academic Press: New York, 1971.
(3) Jeener, J.; Meier, B. H.; Bachmann, P.; Ernst, R. R. *J. Chem. Phys.* **1979**, *71*, 4546.
(4) Kumar, A.; Wagner, G.; Ernst, R. R.; Wüthrich, K. *J. Am. Chem. Soc.* **1981**, *103*, 3654.
(5) Bothner-By, A. A.; Stephens, R. L.; Lee, J.; Warren, C. D.; Jeanloz, R. W. *J. Am. Chem. Soc.* **1984**, *100*, 811.
(6) Ernst, R. R.; Bodenhausen, G.; Wokaun, A. *Principles of NMR in One and Two Dimensions*; Clarendon Press: Oxford, 1987.
(7) Karplus, M. *J. Chem. Phys.* **1959**, *30*, 11.
(8) Bystrov, V. F. *Prog. NMR Spectrosc.* **1976**, *10*, 41.
(9) Wüthrich, K. *NMR of Proteins and Nucleic Acids*; Wiley-Interscience: 1986.
(10) Crippen, G. M.; Havel, T. F. *Distance Geometry and Molecular Conformation*; John Wiley and Sons: New York, 1988.
(11) Brooks, C. L., III; Karplus, M.; Pettitt, B. M. *Proteins: A Theoretical Perspective of Dynamics, Structure, and Thermodynamics*; John Wiley and Sons: New York, 1987.
(12) Olejniczak, E. T.; Dobson, C. M.; Karplus, M.; Levy, R. M. *J. Am. Chem. Soc.* **1984**, *106*, 1923.
(13) Woessner, D. E. *J. Chem. Phys.* **1962**, *37*, 647.
(14) Kowalewski, J. *Annu. Rep. NMR Spectrosc.* **1990**, 22.
(15) Lipari, G.; Szabo, A. *J. Am. Chem. Soc.* **1982**, *104*, 4546.
(16) London, R. E.; Avitable, J. *J. Am. Chem. Soc.* **1978**, *100*, 7159.
(17) Levy, R. M.; Karplus, M.; Wolynes, P. G. *J. Am. Chem. Soc.* **1981**, *103*, 5998.
(18) Westlund, P. O.; Lynden-Bell, R. M. *J. Magn. Reson.* **1987**, *72*, 522.
(19) Farmer, B. T., II; Macura, S.; Brown, L. R. *J. Magn. Reson.* **1988**, *80*, 1.
(20) Hoch, J. C.; Dobson, C. M.; Karplus, M. *Biochemistry* **1985**, *24*, 3831.
(21) Hoch, J. C.; Dobson, C. M.; Karplus, M. *Biochemistry* **1982**, *21*, 1118.

0002-7863/92/1514-2289$03.00/0

motion was examined.

The present theoretical study analyzes the effect of subnanosecond internal motions on proton–proton cross relaxation. The cyclic decapeptide antamanide (-Val[1]-Pro[2]-Pro[3]-Ala[4]-Phe[5]-Phe[6]-Pro[7]-Pro[8]-Phe[9]-Phe[10]-), infinitely dilute in chloroform, is used as the example. This molecule was chosen because it is of intermediate size and because a number of recent experimental investigations is documented.[22-24] The analysis is based on an 800-ps molecular dynamics (MD) simulation, an order of magnitude longer than those used in earlier cross-relaxation studies. In section 2, an overview is given of NMR dipolar cross relaxation and its dependence on motional processes on different time scales. Details of the molecular dynamics simulation are given in section 3. In section 4, the molecular dynamics trajectory is evaluated with respect to proton cross relaxation. Two order parameters, one characterizing distance fluctuations and one reorientational disorder, are introduced which allow the description of the effects of internal mobility on NOESY and ROESY relaxation rates. These effects are discussed for antamanide in section 5. In section 6, a protocol is proposed for the extraction of order parameters and internal motional correlation times by a comparison of experimental NOESY and ROESY data.

2. Correlation Functions and NMR Cross-Relaxation Rates

In this section we relate the NMR dipole–dipole cross-relaxation rate constants Γ_{kl} in laboratory-frame (NOESY) and rotating-frame experiments (ROESY) to the motional correlation functions which contain contributions from overall isotropic tumbling and from intramolecular motion. In the laboratory frame, the transfer rate constant Γ_{kl}^{NOE} of z magnetization from spin I_l to spin I_k

$$\langle I_{lz}\rangle \xrightarrow{\Gamma_{kl}^{NOE}} \langle I_{kz}\rangle \tag{1a}$$

is determined by the time-modulated dipolar interaction of spins k and l and can be written in terms of the spectral densities $J_{kl}(\omega)$[6]

$$\Gamma_{kl}^{NOE} = q\left[-\frac{1}{2}J_{kl}(0) + 3J_{kl}(2\omega_0)\right] \tag{2a}$$

where $q = (1/10)(\mu_0/4\pi)^2\gamma^4\hbar^2$, μ_0 is the magnetic field constant $[4\pi\cdot10^{-7}$ (V s)/(A m)], γ is the gyromagnetic ratio, and ω_0 is the Larmor frequency of the examined spin species. The corresponding rate constant Γ_{kl}^{ROE}, for the 2D ROESY experiment,[5] where transversal magnetization components are allowed to cross-relax in the presence of a spin-lock field

$$\langle I_{lx}\rangle \xrightarrow{\Gamma_{kl}^{ROE}} \langle I_{kx}\rangle \tag{1b}$$

is

$$\Gamma_{kl}^{ROE} = q\left[J_{kl}(0) + \frac{3}{2}J_{kl}(\omega_0)\right] \tag{2b}$$

The rate constants Γ_{kl}^{NOE} and Γ_{kl}^{ROE} are experimentally accessible through the cross-peak intensities in 2D NOESY and 2D ROESY spectra.[6,9]

Dipolar relaxation is determined by the well-known time-dependent dipole coupling Hamiltonian

$$\mathcal{H}^D(t) = (24\pi/5)^{1/2}\frac{\mu_0}{4\pi}\hbar\sum_{(kl)}\gamma_k\gamma_l\sum_{m=-2}^{2}(-1)^m T_{2,-m}^{(kl)} Y_{2m}(\theta_{kl}^{lab}(t),\varphi_{kl}^{lab}(t))/r_{kl}^3(t) \tag{3}$$

where $T_{2,-m}^{(kl)}$ is an irreducible tensor operator of rank 2 and $Y_{2m}(\theta_{kl}^{lab}(t),\varphi_{kl}^{lab}(t))$ a spherical harmonics expressing the interaction between the two spins I_k and I_l with separation r_{kl}. The spectral density $J_{kl}(\omega)$ can be written as the Fourier transform of the correlation functions of the different spherical harmonics in eq 3. For motional processes in an isotropic medium, the correlation functions become independent of the quantum number m of the spherical harmonics $Y_{2m}(\theta(t),\varphi(t))$ involved. We have then

$$J_{kl}(\omega) = \int_{-\infty}^{\infty} C_{kl}(t)\exp(-i\omega t)\,dt \tag{4a}$$

with

$$C_{kl}(t) = 4\pi\left\langle \frac{Y_{20}(\theta_{kl}^{lab}(t_0+t))\,Y^*_{20}(\theta_{kl}^{lab}(t_0))}{r_{kl}^3(t_0+t)r_{kl}^3(t_0)}\right\rangle \tag{4b}$$

In the numerical calculation, the averaging expressed by the angular brackets is evaluated as an average over the time t_0, assuming an ergodic process. The angle $\theta_{kl}^{lab}(t)$ is the angle made by $\mathbf{r}_{kl}(t)$ with respect to the external static magnetic field applied along the z axis.

It is assumed in the following analysis that the overall molecular tumbling and intramolecular motions are uncorrelated. Although this may not strictly be true in experiments and in the simulation, it is expected to be a good approximation for large molecules and internal motions that have little effect on the moments of inertia of the entire molecule such as motions of individual side chains. The correlation function $C_{kl}(t)$ can then be written as a product[25]

$$C_{kl}(t) = C^{tumbling}(t)\,C_{kl}^{internal}(t) \tag{5}$$

For isotropic diffusional tumbling, $C^{tumbling}(t)$ is given by

$$C^{tumbling}(t) = e^{-|t|/\tau_c} \tag{6}$$

where τ_c is the overall rotational tumbling correlation time, which is related to the rotational diffusion constant D by $\tau_c = 1/(6D)$.

The internal correlation function $C_{kl}^{internal}(t)$ can be expressed in the form

$$C_{kl}^{internal}(t) = \frac{4\pi}{5}\sum_{m=-2}^{2}\left\langle \frac{Y_{2m}(\theta_{kl}^{mol}(t_0+t),\phi_{kl}^{mol}(t_0+t))\,Y^*_{2m}(\theta_{kl}^{mol}(t_0),\phi_{kl}^{mol}(t_0))}{r_{kl}^3(t_0+t)\,r_{kl}^3(t_0)}\right\rangle = \left\langle \frac{P_2(\cos\chi_{kl}(t))}{r_{kl}^3(t_0+t)\,r_{kl}^3(t_0)}\right\rangle \tag{7}$$

where the addition theorem of spherical harmonics has been used to obtain the second equality. Here $P_2(x) = (3x^2-1)/2$ is the second rank Legendre polynomial, and $\chi_{kl}(t)$ describes the angle between the internuclear vectors $\mathbf{r}_{kl}(t_0)$ and $\mathbf{r}_{kl}(t_0+t)$, defined by the spherical coordinates r_{kl}, θ_{kl}^{mol}, and ϕ_{kl}^{mol} in a molecule-fixed frame. The averages in the angular brackets can be calculated from the coordinate sets obtained from the molecular dynamics trajectory.

The product form of the correlation function in eq 5 has consequences for the observability of intramolecular mobility: In the case of internal motion that is much faster than the overall tumbling ($\tau_{internal} \ll \tau_c$) but does not lead to a complete decay of $C_{kl}^{internal}(t)$ for $t \to \infty$, the cross-relaxation rate is insensitive to $\tau_{internal}$.[15] The motional influence reflects the spatial restriction of the motion of the internuclear vectors and can be characterized in terms of order parameters. The radial dependence of the cross-relaxation rate, for example, is manifested in this domain by a $\langle 1/r_{kl}^3\rangle^2$ term. On the other hand, if $\tau_{internal}$ is of the same order of magnitude as τ_c, the relaxation rate depends on the internal motional time scale.

Slow conformational changes for $\tau_{internal} \gg \tau_c$ lead to an averaging of the relaxation rate constants; that is

$$\Gamma_{kl}^{average} = \int_{X_0} p(\mathbf{X})\,\Gamma_{kl}(\mathbf{X})\,d\mathbf{X} \tag{8}$$

where the integration extends over the conformational space $\mathbf{X}_0$ with the probability distribution $p(\mathbf{X})$ for conformations $\mathbf{X}$. In $\Gamma_{kl}^{average}$, the radial average takes the form $\langle 1/r_{kl}^6\rangle$, since $\Gamma_{kl}(\mathbf{X})$

(22) Burgermeister, W.; Wieland, T.; Winkler, R. *Eur. J. Biochem.* **1974**, *44*, 311.
(23) Kessler, H.; Griesinger, C.; Lautz, J.; Müller, A.; van Gunsteren, W. F.; Berendsen, H. C. J. *J. Am. Chem. Soc.* **1988**, *110*, 3394.
(24) Blackledge, M.; Brüschweiler, R.; Griesinger, C.; Ernst, R. R. To be submitted for publication.
(25) Wallach, D. *J. Chem. Phys.* **1967**, *47*, 5258.

is proportional to $r_{kl}(\mathbf{X})^{-6}$. The cross-relaxation rate is again insensitive to the rate of internal motion in this regime. The tumbling time τ_c therefore acts as a band-pass filter for the observable time scales of the internal motion. It should be noted that slow internal motion can induce additional relaxation in rotating frame experiments when isotropic components of the total spin Hamiltonian, such as chemical shifts or scalar spin–spin couplings, are modulated by these motional processes.[26,27]

Slow conformational averaging of the cross-relaxation rates is indeed relevant for antamanide. Experiments indicate backbone conformational dynamics involving hydrogen bond breaking and formation on a time scale of the order of 10^{-5} s at room temperature.[24] This fact prevents a direct quantitative comparison of calculated and observed cross-relaxation rates since the 800-ps molecular dynamics trajectory generally remained in the neighborhood of a single backbone conformation **X** and therefore samples only part of the experimentally accessible conformational space $\mathbf{X}_0$ of the antamanide molecule. The discussion in this paper focuses on the rapid motions influencing the relaxation rate constant $\Gamma_{kl}(\mathbf{X})$ for a backbone conformation **X** and its conformational neighborhood.

3. Molecular Dynamics Simulation and Data Analysis

3.1. Atomic Model and Potential Function. The applied microscopic model of antamanide in a chloroform solution includes explicitly all heavy atoms and all hydrogen atoms of the antamanide molecule. The empirical energy function contains terms corresponding to internal bonded interactions (bond stretching, angle bending, dihedral angle, and improper dihedral angle potential terms) and external nonbonded interactions (van der Waals and electrostatic terms). For the amino acid residues the force field parameters of "parallh19" have been used. Chloroform was represented by three chlorine atoms attached to an extended carbon atom that contained the hydrogen atom. Bond length and bond angle potentials are introduced; the parameters for the nonbonded potentials were taken from ref 28. All degrees of freedom of antamanide and of chloroform were allowed to vary during the trajectory, except for the rapid stretching vibrations of bonds involving hydrogen atoms with $\tilde{\nu} \approx 3000$ cm^{-1}; they were treated as rigid by use of the SHAKE algorithm.[29] An integration-time step of 1 fs in the Verlet algorithm was used to compute the trajectory. An atom-based cutoff of 8 Å with a switching function was used for all nonbonded interactions; a shifting function was applied to the electrostatic interactions to remove any discontinuity due to the truncation. The trajectories were computed using the program CHARMM.[30]

3.2. Equilibration Procedure and Molecular Dynamics Simulation. The initial coordinates for the heavy atoms of antamanide were taken from the X-ray structure of ref 31. The hydrogen positions were derived by the CHARMM subroutine HBUILD.[32] The initial structure was first refined in vacuum by energy minimization in the presence of harmonic proton–proton distance constraints corresponding to the NOE cross-relaxation rates obtained from 2D NOESY experiments,[24] followed by further energy minimization in the absence of the NOE distance constraints. The antamanide molecule was then embedded in an equilibrated cubic box of chloroform molecules with a side length of 24.25 Å, and the chloroform molecules overlapping with antamanide were removed. There are 514 atoms in the resulting system, consisting of one antamanide and 88 chloroform molecules. This would correspond to a 0.1 M concentration of antamanide in chloroform. Periodic boundary conditions were applied using the IMAGE facility of CHARMM to remove spurious edge effects.[26] The system was equilibrated by periodically rescaling the velocities for 100 ps at 300 K followed by 50 ps at 250 K. Molecular dynamics without external NOE constraints was used during the equilibration and the actual calculation of the trajectories. During the equilibration period, the average temperature was allowed to stabilize at 250 K. During the production trajectory with a total length of 800 ps, the temperature first decreased slightly to 245 K and increased toward the end of the trajectory to 260 K. No rescaling of the velocities was applied. The computation of the complete trajectory required 250 h on a Silicon Graphics IRIS 220. The conformation of antamanide after 400 ps MD simulation is shown stereographically in Figure 1.

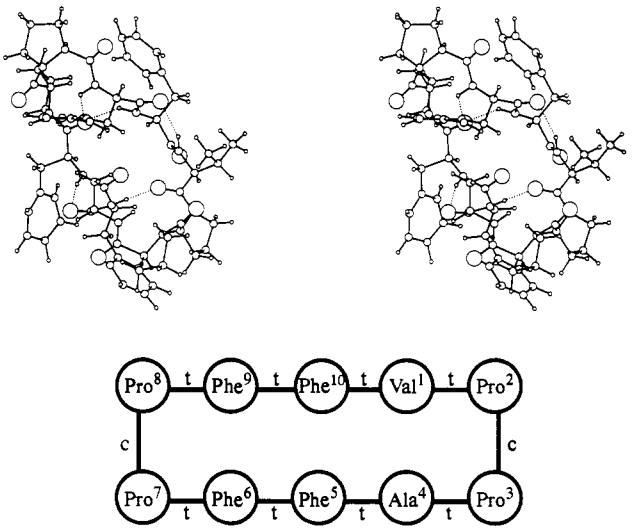

Figure 1. (a, top) Stereographic stick and ball picture of the antamanide structure after 400-ps MD simulation (all atoms). The dashed lines correspond to hydrogen bonds. The numbering of the amino acid residues proceeds clockwise with Pro^8 in the upper left and Pro^2 in the lower right corner. (b, bottom) Schematic drawing of the antamanide cycle, which emphasizes its pseudo-C_2 symmetry with c designating a cis peptide bond, t designating trans peptide bonds.

3.3. Data Analysis. To compute the internal correlation functions $C_{kl}^{internal}(t)$ in the molecule-fixed frame with eqs 5–7, it is necessary to separate the internal motions from the overall tumbling. For that purpose each conformation was translated and reoriented to give the best mass-weighted least-squares fit for all atoms with respect to a reference structure which was chosen as the conformation of antamanide, shown in Figure 1, obtained in the middle of the production trajectory (after 400 ps). Since no large conformational excursions take place during the entire 800-ps trajectory, the molecule-fixed frame is unambiguously defined by this method. The peptide bonds in the reference structure of Figure 1 are trans except for the two bonds Pro^2–Pro^3 and Pro^7–Pro^8 which are cis. The structure shows five hydrogen bonds: Val^1NH–Phe^9O, Phe^5NH–Val^1O, Phe^6NH–Ala^4O, Phe^9NH–Phe^6O, and Phe^{10}NH–Phe^6O. The reference structure has a root mean square deviation from the X-ray structure of 1.4 Å for the main chain and 2.5 Å for all heavy atoms. The corresponding root mean square deviations from the structure minimized with NOE constraints are 1.2 and 2.3 Å, respectively. This is to be compared with the differences between X-ray and NOE-minimized structures; they are 1.2 and 1.4 Å, respectively.

The overall rotational correlation time, τ_c, needed for the computation of the NMR relaxation rates (see eqs 5 and 6), was estimated from the rotational diffusion of the antamanide molecule during the 800-ps trajectory. For this purpose, the three autocorrelation functions $C_i(t) = \langle \mathbf{e}_i(0)\mathbf{e}_i(t)\rangle$, $i = x, y, z$, of the inertia tensor of the molecule were analyzed. The quantities $\mathbf{e}_i$ represent the unit vectors pointing along the principle axes of the inertia tensor of the antamanide molecule expressed in a laboratory-fixed frame. The three rotational correlation functions $C_i(t)$ of the molecule can be approximated by the same exponential function $C_i(t) = \exp\{-t/3\tau_c\}$ with the correlation time $\tau_c \simeq 200$ ps. Al-

(26) Abragam, A. *Principles of Nuclear Magnetism*; Clarendon Press: Oxford, 1961; pp 308–309.
(27) Deverell, C.; Morgan, R. E.; Strange, J. H. *Mol. Phys.* **1970**, *18*, 553.
(28) Jorgensen, W. L. *J. Am. Chem. Soc.* **1989**, *111*, 755.
(29) Ryckaert, J. P.; Ciccotti, G.; Berendsen, H. J. C. *J. Comp. Phys.* **1977**, *23*, 327.
(30) Brooks, B. R.; Bruccoleri, R. E.; Olafsen, B. D.; States, D. J.; Swaminathan, S.; Karplus, M. *J. Comput. Chem.* **1983**, *4*, 187.
(31) Karle, L. L.; Wieland, T.; Schermer, D.; Ottenheym, H. C. J. *Proc. Acad. Sci. U.S.A.* **1979**, *76*, 1532.
(32) Brünger, A.; Karplus, M. *Proteins* **1988**, *4*, 148.

Table I. Backbone Torsional Angles: Averages and Root Mean Square (rms) Fluctuations

angle	average value, deg	rms fluctuation, deg	X-ray structure, deg	NOE-mimimized structure, deg
φ_1	−105.6	±12.7	−112.9	−116.2
ψ_1	−177.0	±8.0	158.1	179.4
φ_2	−89.2	±7.0	−63.9	−91.5
ψ_2	154.9	±6.4	161.2	127.5
φ_3	−95.6	±5.3	−79.5	−113.5
ψ_3	53.1	±8.1	−20.5	38.8
φ_4	−111.4	±8.4	−103.4	−122.6
ψ_4	−53.5	±7.8	−21.8	37.0
φ_5	88.7	±8.1	70.2	−25.7
ψ_5	−47.6	±11.3	29.5	62.0
φ_6	−97.4	±17.3	−78.2	−130.9
ψ_6	−177.3	±8.8	161.0	140.0
φ_7	−88.6	±6.7	−62.0	−43.9
ψ_7	153.2	±6.4	160.1	128.3
φ_8	−95.5	±5.5	−91.8	−114.3
ψ_8	53.0	±7.7	−3.8	43.3
φ_9	−110.1	±7.5	−101.1	−119.9
ψ_9	−54.5	±7.0	−21.8	−15.3
φ_{10}	88.3	±7.8	56.3	8.0
ψ_{10}	−42.5	±10.7	47.8	60.7

though only the very initial parts of the correlation functions can be determined from the MD run, it appears that antamanide in the computer simulation undergoes isotropic small-step rotational diffusion. The factor 3 in the above relation for $C_i(t)$ occurs due to the fact that the decay constant τ of $\langle \mathbf{e}_i(0)\mathbf{e}_i(t)\rangle$ is related to the diffusional rate constant D by $\tau = 1/2D$ while τ_c in eq 6 is given by $\tau_c = 1/6D$, and thus $\tau = 3\tau_c$.[33] From NMR relaxation measurements, a value of $\tau_c = 600$ ps was found.[24] The discrepancy may arise from the poor statistics for the tumbling process (due to the relatively short observation time) and possibly from an inaccurate description of the interaction between antamanide and the solvent molecules. For the subsequent analysis of NMR parameters, the experimental value $\tau_c = 600$ ps was used.

For the analysis of internal motions and NMR cross-relaxation rates, 40 000 conformations were selected at time intervals of 20 fs. The proton NMR frequency was set to $\omega_0/2\pi = 500$ MHz, which corresponds to a magnetic field strength of 11.74 T. The spectral densities $J_{kl}(n\omega_0)$ ($n = 0, 1, 2$) were calculated by numerical integration of eq 3, using the correlation functions $C_{kl}(t)$ obtained from eqs 5–7. An integration time limit of 400 ps was introduced, since the correlation functions became more uncertain with increasing delay time.

4. Parameter Fluctuations and Correlation Functions

This section describes the molecular dynamics trajectory of antamanide in terms of average properties and histograms in view of the analysis of NMR cross-relaxation rates in section 5.

4.1. Torsional Angle and Distance Fluctuations. The average backbone torsional angles φ_i and ψ_i and their fluctuations, calculated from the molecular dynamics trajectory, are collected in Table I. The values reflect the pseudo-C_2 symmetry of the antamanide ring (Figure 1b) with $\varphi_{i+5} \simeq \varphi_i$ and $\psi_{i+5} \simeq \psi_i$, $i = 1, ..., 5$. The largest deviations violating the pseudo-C_2 symmetry are 8° for the pair φ_1,φ_6 and 5° for ψ_5,ψ_{10}. For the backbone of antamanide, the root mean square values of the fluctuations are similar to those observed during vacuum simulations of the interior of proteins.[11] There are no backbone dihedral transitions (e.g. flips of peptide bonds) during the trajectory. The fluctuation behavior shows a pseudosymmetry similar to that of the structure.

A scatter plot of the distance fluctuations $\sigma(r_{kl}) = \langle(r_{kl} - \langle r_{kl}\rangle)^2\rangle^{1/2}$ of proton pairs kl versus the average distances $\langle r_{kl}\rangle$ is shown in Figure 2. The histogram at the bottom of Figure 2 represents the distribution of the interproton distances in antamanide with $r_{kl} < 4.5$ Å, which contribute significantly to the internuclear cross-relaxation rates. The maxima near 1.8, 2.5,

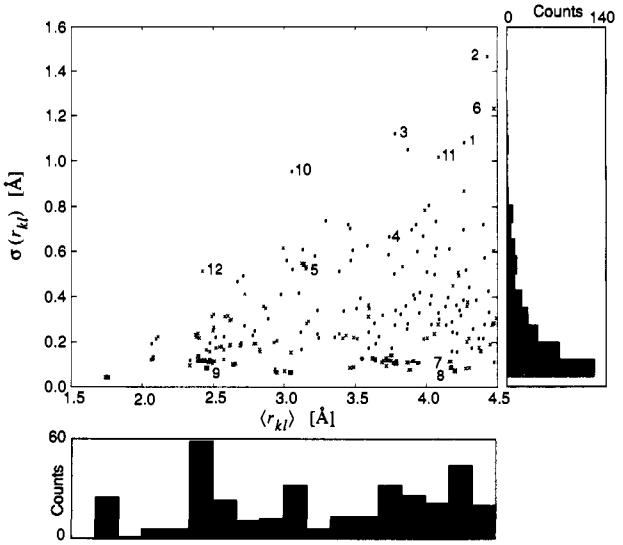

Figure 2. Correlation of proton–proton distances $\langle r_{kl}\rangle$ of antamanide for $r < 4.5$ Å with the corresponding distance fluctuations $\sigma(r_{kl}) = \langle(r_{kl} - \langle r_{kl}\rangle)^2\rangle^{1/2}$ calculated from the 800-ps MD trajectory. The two histograms characterize the distribution of $\langle r_{kl}\rangle$ (bottom) and $\sigma(r_{kl})$ (right), respectively. The numbered crosses refer to the proton pairs in Table II.

and 3.1 Å correspond, among others, to geminal, gauche, and antiperiplanar vicinal proton pairs, respectively. Figure 2 demonstrates a nearly linear increase of the maximum fluctuation amplitude with the average separation of the protons, though at all distances the minimum fluctuations approach zero. This is a feature characteristic of relatively rigid extended systems without backfolded regions that could approach parts of the molecule distant along the polypeptide chain. Thus, Figure 2 may be atypical for a folded protein. Figure 2 gives also a histogram of the distance fluctuations. It is peaked in the range between 0.05 and 0.1 Å and decays rapidly toward larger fluctuations. The average value of the fluctuation for the 356 proton pairs fulfilling $\langle r_{kl}\rangle < 4.5$ Å is $\bar{\sigma} = 0.24$ Å. It should be noted that the maximum fluctuation amplitude strongly depends on the duration of the trajectory and some values of Figure 2 may increase for longer time scales. Large-amplitude side-chain motions are rare on the time scale of the 800-ps molecular dynamics trajectory. As an exception, occasional 120° rotations for the side-chain torsion angle χ_2 of Phe[6] (three transitions) and Phe[9] (two transitions) were observed during the simulation.

Twelve illustrative proton pairs corresponding to different distances are numbered in Figure 2 and identified in the first column of Table II; the same numbering is used in subsequent figures. Table II contains the numerical values of various quantities discussed in the following for these and other selected proton pairs. The first part of Table II contains 12 selected proton pairs involved in larger scale motions. The second part shows some selected intraresidual, sequential, and transannular backbone–backbone proton pairs. It is apparent that all proton pairs with a large fluctuation amplitude $\sigma(r_{kl})$ involve at least one side-chain proton; examples are the pairs Phe[5]$H_{\beta 1}$–Phe[6]$H_{\epsilon 1}$ {1}, Phe[6]$H_{\delta 1}$–Pro[7]$H_{\delta 2}$ {6}, Phe[6]NH–Phe[6]$H_{\delta 2}$ {3}, Pro[8]$H_{\delta 1}$–Phe[9]$H_{\epsilon 1}$ {10}, and Phe[9]NH–Phe[9]$H_{\delta 1}$ {12}. By contrast, pairs involving only main-chain protons have small fluctuations, examples are Val[1]NH–Phe[5]NH and Phe[10]H_α–Val[1]NH. The numbers in braces {··}, defined in Table II, refer to the numbering of points in the figures.

The approximate symmetry in main chain dihedral angles, introduced by the symmetrical initial conformation used for the molecular dynamics simulation, is reflected in the distances and fluctuation amplitudes shown in Figure 3. Symmetric pairs of sequential interresidue backbone distances behave similarly. The backbone remains approximately symmetric during the entire simulation and this symmetry is retained also in the fluctuation amplitudes $\sigma(r_{kl})$.

There are numerous proton pairs for which the distance and angle distribution of the trajectory shows a single peak. This

(33) McQuarrie, D. A. *Statistical Mechanics*; Harper & Son: New York, 1976; p 398.

Table II

label	proton pair	$\langle r \rangle$, Å	σ_r, Å	S^2	S_Ω^2	S_r^2	$S_\Omega^2 S_r^2$	Γ_{NOE}^{dyn}, s^{-1}	$\Gamma_{NOE}^{dyn}/\Gamma_{NOE}^{stat}$	Γ_{ROE}^{dyn}, s^{-1}	$\Gamma_{ROE}^{dyn}/\Gamma_{ROE}^{stat}$	$\Gamma_{NOE}^{dyn}/\Gamma_{ROE}^{dyn}$	τ_{kl}, ps
1	$Phe^5H_{\beta 1}$–$Phe^6H_{\epsilon 1}$	4.27	1.09	0.27	0.44	0.59	0.26	0.0012	−0.34	0.018	1.22	0.063	41
2	$Phe^5H_{\beta 2}$–$Phe^6H_{\delta 2}$	4.43	1.47	0.36	0.60	0.52	0.31	0.0044	-1.62	0.041	3.41	0.108	107
3	Phe^6NH–$Phe^6H_{\delta 2}$	3.78	1.12	0.30	0.37	0.55	0.21	0.0146	−2.06	0.072	2.30	0.204	150
4	Phe^6H_α–$Phe^6H_{\delta 2}$	3.74	0.67	0.16	0.31	0.59	0.18	0.0057	−0.75	0.022	0.66	0.259	43
5	$Phe^6H_{\beta 1}$–$Phe^6H_{\delta 1}$	3.16	0.53	0.22	0.22	0.80	0.17	0.0214	−1.02	0.057	0.62	0.374	150
6	$Phe^6H_{\delta 1}$–$Pro^7H_{\delta 2}$	4.48	1.24	0.36	0.54	0.57	0.31	0.0020	−0.79	0.024	2.11	0.085	86
7	$Phe^6H_{\delta 2}$–Phe^6H_ζ	4.20	0.08	0.36	0.36	1.00	0.36	0.0007	−0.20	0.008	0.46	0.100	104
8	$Phe^6H_{\epsilon 1}$–$Phe^6H_{\epsilon 2}$	4.20	0.07	0.48	0.48	0.99	0.48	−0.0010	0.27	0.009	0.53	−0.115	33
9	$Phe^6H_{\epsilon 2}$–Phe^6H_ζ	2.46	0.09	0.15	0.15	1.00	0.15	0.0551	−0.59	0.122	0.30	0.453	98
10	$Pro^8H_{\delta 1}$–$Phe^9H_{\epsilon 1}$	3.06	0.96	0.54	0.70	0.77	0.54	−0.0311	1.22	0.139	1.25	−0.224	3
11	$Pro^8H_{\delta 1}$–Phe^9H_ζ	4.09	1.02	0.50	0.80	0.62	0.50	−0.0068	1.52	0.031	1.60	−0.217	5
12	Phe^9NH–$Phe^9H_{\delta 1}$	2.43	0.52	0.64	0.73	0.84	0.61	−0.1061	1.04	0.479	1.07	−0.222	5
	Val^1NH–Val^1H_α	2.95	0.07	0.93	0.94	0.99	0.93	−0.0296	0.94	0.1303	0.95	−0.227	1.5
	Val^1NH–Phe^5NH	4.13	0.36	0.89	0.97	0.92	0.89	−0.0044	1.06	0.0190	1.07	−0.227	0.8
	$Phe^{10}H_\alpha$–Val^1NH	3.46	0.09	0.94	0.95	0.99	0.94	−0.0114	0.95	0.0504	0.95	−0.227	0.4
	Pro^2H_α–Pro^3H_α	2.08	0.14	0.91	0.95	0.96	0.91	−0.2577	0.99	1.1308	0.99	−0.228	0.8
	Pro^2H_α–Ala^4NH	2.11	0.23	0.82	0.91	0.91	0.83	−0.2418	1.04	1.0653	1.04	−0.227	0.4
	Pro^3H_α–Ala^4NH	2.83	0.17	0.90	0.94	0.97	0.90	−0.0397	0.98	0.1740	0.98	−0.228	0.5
	Ala^4NH–Ala^4H_α	2.95	0.07	0.94	0.94	0.99	0.94	−0.0295	0.95	0.1295	0.95	−0.228	0.6
	Ala^4NH–Phe^5NH	2.52	0.22	0.84	0.91	0.93	0.84	−0.0814	1.00	0.3579	1.00	−0.228	0.4
	Phe^5NH–Phe^5H_α	2.34	0.10	0.89	0.91	0.98	0.89	−0.1159	0.93	0.5107	0.93	−0.227	1.5
	Phe^5NH–$Phe^{10}NH$	4.35	0.39	0.90	0.97	0.93	0.90	−0.0033	1.07	0.0143	1.07	−0.228	0.4
	Phe^5H_α–Phe^6NH	3.47	0.09	0.92	0.93	0.99	0.92	−0.0111	0.93	0.0490	0.93	−0.227	2.0
	Phe^6NH–Phe^6H_α	2.94	0.08	0.92	0.93	0.99	0.92	−0.0300	0.93	0.1328	0.94	−0.226	2.7
	Pro^7H_α–Pro^8H_α	2.08	0.13	0.92	0.95	0.97	0.92	−0.2542	0.99	1.1188	0.99	−0.227	0.5
	Pro^7H_α–Phe^9NH	2.10	0.22	0.84	0.92	0.91	0.84	−0.2472	1.03	1.0904	1.04	−0.227	0.4
	Pro^8H_α–Phe^9NH	2.83	0.16	0.91	0.94	0.97	0.91	−0.0390	0.97	0.1721	0.98	−0.227	0.7
	Phe^9NH–Phe^9H_α	2.94	0.07	0.94	0.95	0.99	0.94	−0.0307	0.95	0.1351	0.96	−0.227	1.1
	Phe^9NH–$Phe^{10}NH$	2.56	0.23	0.85	0.92	0.93	0.86	−0.0712	1.01	0.3135	1.01	−0.227	0.3
	Phe^9H_α–$Phe^{10}NH$	3.49	0.09	0.95	0.96	0.99	0.95	−0.0110	0.97	0.0485	0.97	−0.227	1.0
	$Phe^{10}NH$–$Phe^{10}H_\alpha$	2.34	0.10	0.91	0.92	0.98	0.91	−0.1192	0.94	0.5252	0.94	−0.227	0.9

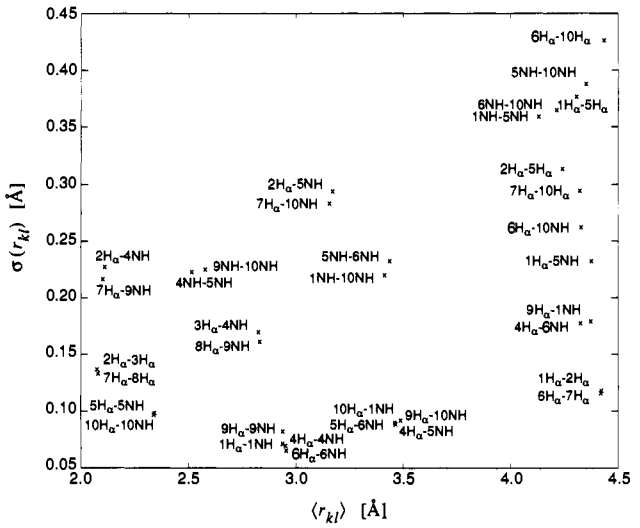

Figure 3. Section of Figure 2 restricted to backbone proton pairs. The pseudo-C_2 symmetry of the molecule is manifested in the pairing of the crosses.

indicates that there is a single-minimum potential function describing their short-time motion. Such behavior occurs particularly for backbone protons. An example is the pair Val^1NH–Phe^5NH for which the almost Gaussian distance distribution and the skew angular distribution are shown in parts a and b of Figure 4. On the other hand, there are some proton pairs with double-peak distributions, which reflect a local multiple minimum potential. A typical case is presented in parts c and d of Figure 4 for the pair Phe^6NH–$Phe^6H_{\delta 2}$ {3}. The double minimum potential originates from 120° flips of the χ_2 torsion angle of the phenyl ring of Phe^6 during the trajectory, although the statistics is rather poor due to the small number of torsional transitions during the limited observation time. In the case of the pair $Pro^8H_{\delta 1}$–$Phe^9H_{\epsilon 1}$ {10}, the two distinct sites are unequally populated (Figure 4e,f). The behavior observed here for the interpair parameters is analogous to that found for the positional fluctuations of atoms in proteins.[34]

4.2. Correlation Functions and Order Parameters. To evaluate the expressions for the cross-relaxation rates, given in section 3, it is necessary to compute the correlation functions for individual proton pairs from the molecular dynamics trajectory. The correlation defined by eq 7 refers specifically to the dipolar interaction of two spins k and l. A typical example is presented in Figure 5a for the proton pair Val^1NH–Phe^5NH. It shows a fast initial decay within a few picoseconds and then reaches a "plateau value" of 89% of the initial value. On a much longer time scale, a further decrease of the correlation may be expected as a consequence of slow motional processes that are not sampled by the trajectory. Figure 5b shows an example of a differently behaved correlation function for the proton pair Phe^6NH–$Phe^6H_{\delta 2}$ (3). Here a plateau value is not reached within the time range shown in the figure. The results can be represented by two correlation times, a short one ($\tau \cong 1$ ps) describing the local motion (similar to that shown in Figure 5a) and a longer one that characterizes the phenyl ring rotation ($\tau \cong 100$ ps). Since the phenyl ring flips represent rare events on the 800-ps time scale, the probability distributions in Figures 4c–f and the decay behavior of the correlation function in Figure 5b are subjected to large statistical errors.

The limiting value for $t \rightarrow \infty$ of the correlation function $C_f(t)$ of an arbitrary function $f(t)$ reflects the extent of invariant order of the system with respect to $f(t)$ and can be characterized by an order parameter S_f^2 [15] defined by

$$S_f^2 = \lim_{t\to\infty} \frac{\langle f(t) f^*(0) \rangle}{\langle |f(0)|^2 \rangle} = \frac{|\langle f \rangle|^2}{\langle |f|^2 \rangle} \tag{9}$$

where by definition $0 \le S_f^2 \le 1$. Thus, a correlation function of the form of Figure 5a can be approximated by the expression

$$C_f(t) \simeq \langle |f|^2 \rangle \{S^2 + (1 - S^2) e^{-|t|/\tau}\} \tag{10}$$

with τ being an intramolecular correlation time that characterizes the "effective" decay of correlation due to internal motion.[15]

For the type of relaxation shown in Figure 5b, a two-step disordering can be postulated involving two statistically inde-

(34) Ichyie, T.; Karplus, M. *Proteins* **1987**, *2*, 236.

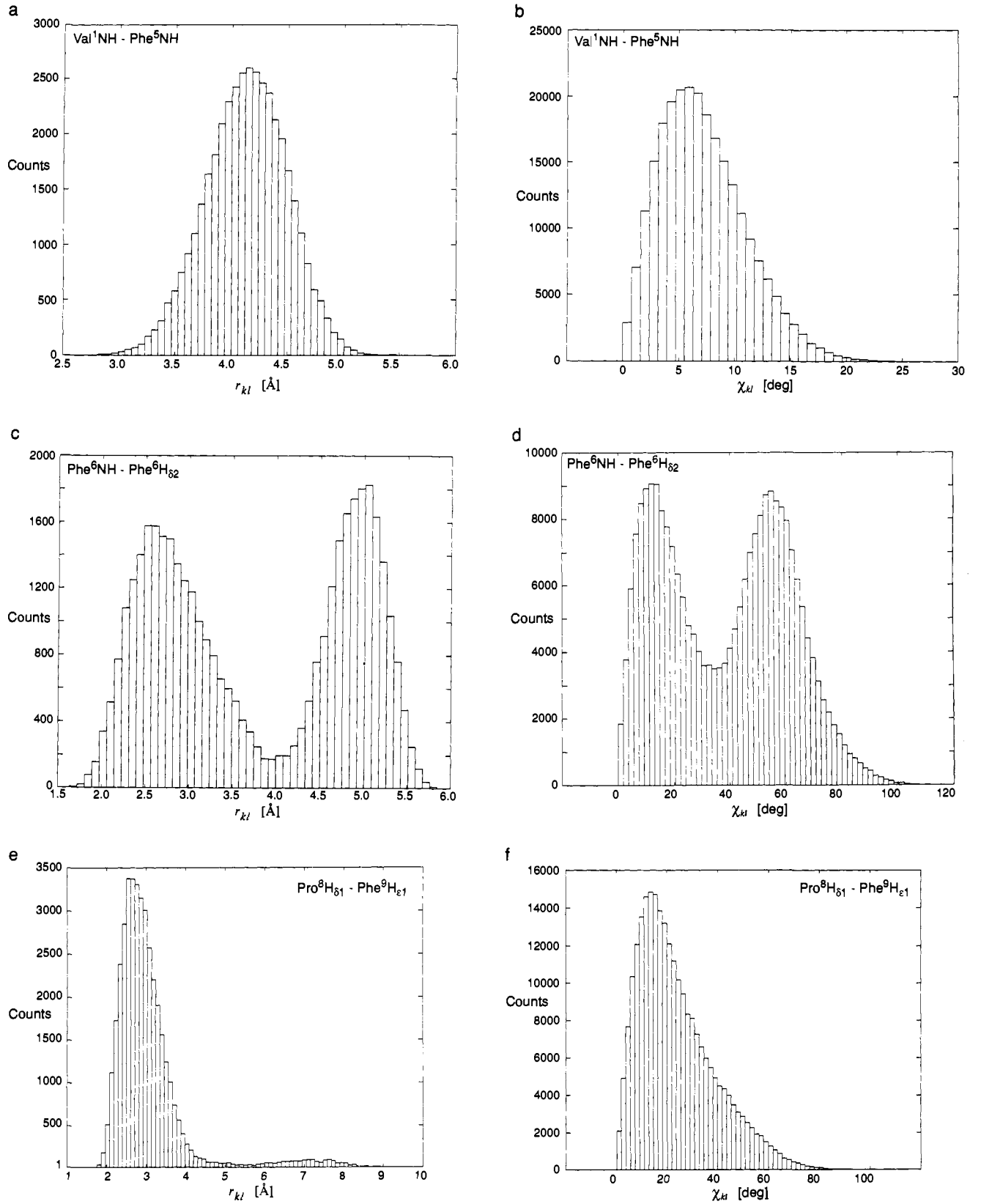

Figure 4. Distance and director distributions along the MD trajectory calculated in a molecule-fixed frame of the proton pairs Val¹NH–Phe⁵NH (a, b), Phe⁶NH–Phe⁶H$_{\delta 2}$ (c, d), and Pro⁸H$_{\delta 1}$–Phe⁹H$_{\varepsilon 1}$ (e, f) in antamanide.

pendent processes with S^2_{fast}, τ_{fast} and S^2_{slow}, τ_{slow}. According to ref 35, we write for $\tau_{\text{fast}} \ll \tau_c$

$$C_f(t) \cong \langle |f|^2 \rangle S^2_{\text{fast}}[S^2_{\text{slow}} + (1 - S^2_{\text{slow}})e^{-|t|/\tau_{\text{slow}}}] \qquad (11)$$

The dipolar correlation function $C_{kl}^{\text{internal}}(t)$, defined in eq 7, consists of a sum of correlation functions of five individual functions

$$f^m_{kl}(t) = \frac{Y_{2m}(\theta^{\text{mol}}_{kl}(t),\phi^{\text{mol}}_{kl}(t))}{r^3_{kl}(t)} \qquad (12)$$

(35) Clore, G. M.; Szabo, A.; Bax, A.; Kay, L. E.; Driscoll, P. C.; Gronenborn, A. M. *J. Am. Chem. Soc.* **1990**, *112*, 4989.

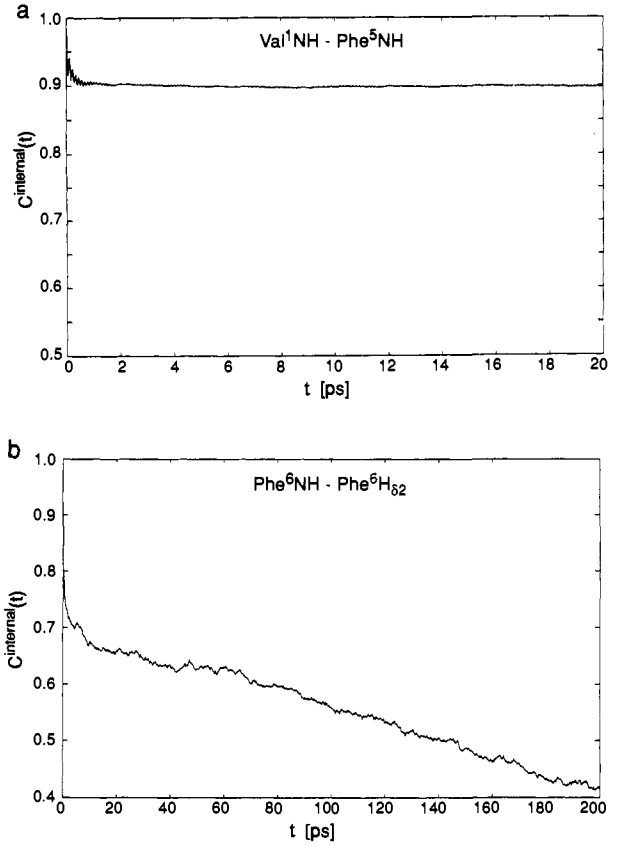

Figure 5. Internal correlation functions $C^{internal}(t)$ (eq 7) of (a) proton pair Val¹NH–Phe⁵NH and (b) proton pair Phe⁶NH–Phe⁶H$_{\delta 2}$ in antamanide.

that can be determined from the trajectory. Assuming that $C_{kl}^{internal}(t)$ has the form of eq 10, the spectral density is given by

$$J_{kl}(\omega) = \int_{-\infty}^{\infty} C_{kl}^{internal}(t)\, e^{-|t|/\tau_c} e^{-i\omega t}\, dt \qquad (13a)$$

$$\simeq \left\langle \frac{1}{r_{kl}^6} \right\rangle S_{kl}^2 \frac{2\tau_c}{1+\omega^2\tau_c^2} + \left\langle \frac{1}{r_{kl}^6} \right\rangle (1 - S_{kl}^2) \frac{2\tau_{tot}}{1+\omega^2\tau_{tot}^2} \qquad (13b)$$

where

$$\frac{1}{\tau_{tot}} = \frac{1}{\tau_c} + \frac{1}{\tau_{kl}}$$

and

$$S_{kl}^2 = \frac{4\pi}{5} \left\langle \frac{1}{r_{kl}^6} \right\rangle^{-1} \sum_{m=-2}^{2} \left| \left\langle \frac{Y_{2m}(\theta_{kl}^{mol}, \phi_{kl}^{mol})}{r_{kl}^3} \right\rangle \right|^2 \qquad (14)$$

The first term in eq 13b depends only on the order parameter S_{kl}^2 and not on the time scale τ_{kl} of the internal motions. The second term, on the other hand, is a function of both S_{kl}^2 and τ_{kl}. S_{kl}^2 is a measure for the degree of spatial restriction of the internuclear vector. It should be noted that the prefactor $\langle 1/r_{kl}^6 \rangle^{-1}$ in eq 14 is not used in a related definition in ref 15.

Histograms of order parameters S_{kl}^2 and correlation times τ_{kl} are given in Figure 6. It is seen that the majority of proton pairs shows order parameters above $S_{kl}^2 = 0.8$. The correlation time τ_{kl} has been estimated by the expression[15]

$$\tau_{kl} = \int_0^{t_{max}} dt \left[\frac{C_{kl}(t)}{C_{kl}(0)} - S_{kl}^2 \right] \Big/ (1 - S_{kl}^2) \qquad (15)$$

For the values shown in Figure 6, t_{max} has been set equal to 20 ps. Most of the internal correlation times τ_{kl} are in a range $0.5 < \tau_{kl} < 1.5$ ps. Some values larger than 20 ps are contained in Table II. They have been obtained by back calculation of the

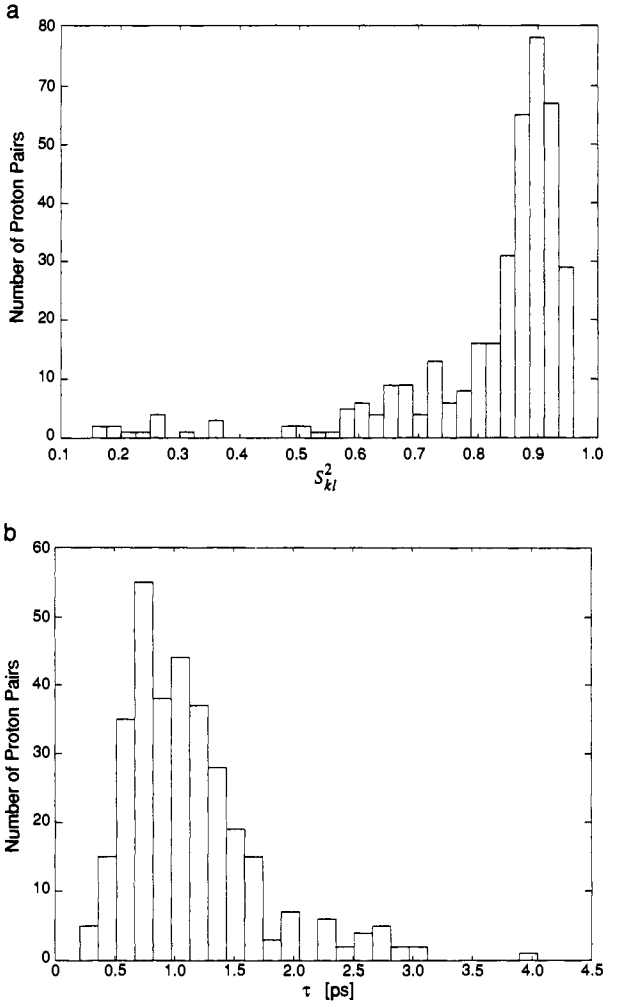

Figure 6. (a) Histogram of the order parameter S_{kl}^2 as defined in eq 14. (b) Histogram of the distribution of internal correlation times τ_{kl}, as defined in eq 15, for proton pairs in antamanide with a cutoff of $\tau_{kl} < 4.5$ ps.

cross-relaxation rates using eqs 2 and 13b.

It should be noted that none of the correlation functions is accurately fitted by a monoexponential decay toward a plateau value. This is reflected also in an observed dependence of the estimated correlation time τ_{kl} on t_{max} using eq 15. However, for many proton pairs the dominant decay takes place in the picosecond range, which cannot be monitored in detail by means of NMR relaxation experiments and is therefore uncritical for the calculation of relaxation parameters. The τ_{kl} values given in the histogram should be interpreted as upper limits of correlation times that contribute significantly to the correlation function. For longer time scale motion, as e.g. present for Phe⁶NH–Phe⁶H$_{\delta 2}$ {3} (Figure 5b), τ_{kl} directly affects the cross-relaxation rate. If a single correlation time for the quantitative description of $C_{kl}^{internal}(t)$ is inadequate, the more general eq 13a has to be used for a numerical evaluation. The simplified eq 13b, however, provides intuitive insight into the interplay between the three quantities S_{kl}^2, τ_c, and τ_{kl}.

The cross-relaxation rate constants of eqs 2a and 2b can be expressed in terms of order parameters and correlation times by means of eq 13b

$$\Gamma_{kl}^{NOE/ROE} = S_{kl}^2 \Gamma_{kl}^{NOE/ROE}(\tau_c) + (1 - S_{kl}^2) \Gamma_{kl}^{NOE/ROE}(\tau_{tot}) \qquad (16)$$

where the rate constants $\Gamma_{kl}^{NOE/ROE}(\tau)$ are defined by

$$\Gamma_{kl}^{NOE}(\tau) = q \left\langle \frac{1}{r_{kl}^6} \right\rangle \left(-\tau + \frac{6\tau}{1 + 4\omega_0^2\tau^2} \right)$$

and

$$\Gamma_{kl}^{ROE}(\tau) = q\left\langle\frac{1}{r_{kl}^6}\right\rangle\left(2\tau + \frac{3\tau}{1+\omega_0^2\tau^2}\right) \qquad (17)$$

respectively. Because $\Gamma_{kl}^{ROE}(\tau)$ monotonously increases with increasing τ and $\tau_{tot} \leq \tau_c$, it follows that Γ_{kl}^{ROE} reaches its maximum in the regime $\tau_{kl} \gg \tau_c$. Such a monotonous behavior does not apply for $\Gamma_{kl}^{NOE}(\tau)$ as the following computations show.

Figure 7 gives a survey of the dependence of the cross-relaxation rates in the laboratory and rotating frames on the relative tumbling correlation time $\tau_c\omega_0$, the internal correlation time $\tau_{kl}\omega_0$, and the order parameter S_{kl}^2. Normalized rate constants $\Gamma_{kl}^{NOE}\omega_0 q^{-1}\cdot\langle 1/r_{kl}^6\rangle^{-1}$ and $\Gamma_{kl}^{ROE}\omega_0 q^{-1}\langle 1/r_{kl}^6\rangle^{-1}$ have been computed by eqs 16 and 17 for two selected order parameters $S_{kl}^2 = 0.7$ and $S_{kl}^2 = 0.2$. The individual curves, plotted against $\tau_c\omega_0$, apply to a fixed product $\tau_{kl}\omega_0$.

The vertical spread of the curves in Figure 7 indicates, for given values of $\tau_c\omega_0$ and S_{kl}^2, the variation of the cross-relaxation rates as a function of the intramolecular mobility time scale. Curve 1 gives the limit for slow internal motion, $\tau_{kl}\omega_0$, $\tau_{kl}/\tau_c \gg 1$, while curve 5 indicates the limit for rapid internal motion, $\tau_{kl}\omega_0$, $\tau_{kl}/\tau_c \ll 1$. When one of these conditions is fulfilled, the cross-relaxation rate becomes insensitive to the actual value of the correlation time τ_{kl}. The two extreme curves 1 and 5 have identical shape and are vertically scaled relative to each other by the order parameter S_{kl}^2.

Parts c and d of Figure 7 visualize the monotonous behavior of Γ_{kl}^{ROE} as a function of all parameters. Increasing overall mobility will invariably decrease the cross-relaxation rate. On the other hand, it is well-known that Γ_{kl}^{NOE} can change sign as a function of $\tau_c\omega_0$. Parts a and b of Figure 7 demonstrate that it can also change sign as a function of $\tau_{kl}\omega_0$ for fixed $\tau_c\omega_0$. The interval $(\tau_c\omega_0)_{min} < \tau_c\omega_0 < (\tau_c\omega_0)_{max}$ within which this can occur depends on the order parameter S_{kl}^2. The relative width of the interval is 1.4 for $S_{kl}^2 = 0.7$, 3.0 for $S_{kl}^2 = 0.2$, and 7.8 for $S_{kl}^2 = 0.05$. Such differential effects between NOESY and ROESY rates might be exploited for an experimental determination of τ_{kl} and S_{kl}^2 as will be discussed in section 6.

For rapid internal motion, $\tau_{kl} \ll \tau_c$, the second term in eq 16 involving τ_{kl} becomes negligibly small compared to the first term, provided that S_{kl}^2 is significantly different from zero and $\omega_0\tau_c \neq 5^{1/2}/2$. This implies that the NMR relaxation rates, computed from eq 2a or 2b, become virtually independent of the rate constants $1/\tau_{kl}$ of the fast internal processes and are determined by τ_c and the order parameters S_{kl}^2 alone.[15] Due to the limited length of the MD trajectory, this situation corresponds to most of the motional processes observed in the antamanide simulation. In this limit, the actual cross-relaxation rate constant Γ_{kl} may be related to a hypothetical cross-relaxation rate constant Γ_{kl}^{stat} for a rigid molecule with average distances $\langle r_{kl}\rangle$

$$\Gamma_{kl} = \langle r_{kl}\rangle^6\left\langle\frac{1}{r_{kl}^6}\right\rangle S_{kl}^2\Gamma_{kl}^{stat} \qquad (18)$$

where Γ_{kl}^{stat} can be calculated via eq 2a or 2b using

$$J_{kl}(\omega) = \frac{1}{\langle r_{kl}\rangle^6}\frac{2\tau_c}{1+\omega^2\tau_c^2} \qquad (19)$$

This is true for cross relaxation in the laboratory frame and in the rotating frame (eqs 2a and 2b, respectively). In this limit, internal motion scales the two cross-relaxation rates uniformly. More specific effects occur when the order parameter S_{kl}^2 fulfills the inequalities $S_{kl}^2 \lesssim 10\tau_{kl}/\tau_c \lesssim 0.1$. Then, the second term in eq 16 can no longer be neglected and cross relaxation becomes sensitive to τ_{kl}.

4.3. Radial and Angular Order Parameters. The order parameters S_{kl}^2 of the dipolar interaction between spins k and l, and correspondingly the trajectory function $f_{kl}^m(t)$ of eq 12, depends on the variation of the internuclear distance $r_{kl}(t)$ as well as on the variation of the angular functions $\theta_{kl}^{mol}(t)$ and $\phi_{kl}^{mol}(t)$. Moreover, eq 13 shows that the cross-relaxation rate constant Γ_{kl} depends not only on the order parameter S_{kl}^2, as defined in eq 14, but also on the distance averaging through the factor $\langle 1/r_{kl}^6\rangle$. Because radial and angular variations have opposite effects on the cross-relaxation rate, as will be shown below, it is desirable to factorize S_{kl}^2 into separate radial and angular contributions. We write S_{kl}^2 as the approximate product

$$S_{kl}^2 \simeq S_{r,kl}^2 S_{\Omega,kl}^2 \qquad (20)$$

where $S_{r,kl}^2$ represents the "radial order" and $S_{\Omega,kl}^2$ the "angular order". The quality of this approximation will be tested below. The two new order parameters are defined by (cf. eqs 7 and 14)

$$S_{r,kl}^2 = \left\langle\frac{1}{r_{kl}^3}\right\rangle^2 \Big/ \left\langle\frac{1}{r_{kl}^6}\right\rangle \qquad (21)$$

and

$$S_{\Omega,kl}^2 = \lim_{t\to\infty}\langle P_2(\cos\chi_{kl}(t))\rangle = \frac{4\pi}{5}\sum_{m=-2}^{2}|\langle Y_{2m}(\theta_{kl},\phi_{kl})\rangle|^2 \qquad (22)$$

Both order parameters are confined to the interval [0,1].

The separation of radial and angular order parameters is useful for describing the different influences of radial and angular order on the NMR cross-relaxation rates. Rapid radial fluctuations lead to an increased cross-relaxation rate since short distances have a stronger weight in the average dipolar interaction $\langle 1/r_{kl}^3\rangle$ than the larger distances. The following two inequalities are strictly applicable:

$$\left\langle\frac{1}{r_{kl}^6}\right\rangle \geq \left\langle\frac{1}{r_{kl}^3}\right\rangle^2 \geq \frac{1}{\langle r_{kl}\rangle^6} \qquad (23)$$

The first inequality implies that for a given distance distribution of a nuclear pair kl, the magnitude of the cross-relaxation rate constant for the case $\tau_{kl} \gg \tau_c$ is always larger than or equal to the rate for $\tau_{kl} \ll \tau_c$ (compare curves 1 and 5 in Figure 7a,b). The second inequality signifies that for both motional regimes the cross-relaxation rates are larger than or equal to the one attributed to a rigid pair with the linearly averaged distance. The equality signs apply only in the absence of internal motion.

Angular fluctuations reduce the cross-relaxation rate because the angular term $P_2(\cos\chi_{kl})$ of the dipolar correlation function is reduced by motional averaging. The angular term is maximal and equal to 1 in the absence of angular motion ($\chi_{kl} = 0$) and smaller than 1 whenever such motion occurs (except for $\chi_{kl} = \pi$).

In eq 20 strict equality holds only when the radical and angular motions are statistically independent. As will be shown below, the correlation between radial and angular dynamics is usually weak in real molecules, due to the presence of many motional degrees of freedom. Even in cases where the correlation is significant, eq 20 may provide a good approximation (see section 4.4). Separation of radial and angular motion for heteronuclear atom pairs is discussed in ref 36.

The effect of the degree of correlation between the two order parameters $S_{\Omega,kl}^2$ and $S_{r,kl}^2$ on S_{kl}^2 is indicated in Figure 8 where the product $S_{\Omega,kl}^2 S_{r,kl}^2$ for different proton pairs is plotted against the total order parameter S_{kl}^2 for antamanide computed from the molecular dynamics trajectory. For $S_{kl}^2 > 0.5$, there are very few significant deviations; for $S_{kl}^2 < 0.5$ the deviations are somewhat larger. Both positive (i.e. $S_{r,kl}^2 S_{\Omega,kl}^2 > S_{kl}^2$) and negative deviations are found. The linear regression correlation coefficient is 0.996. The relatively minor deviations of the points from the diagonal indicate that the interdependence of the two order parameters is weak for most of the proton pairs and that the influences of angular and radial fluctuations are separable for this example. In Figure 9, the contributions of angular and radial fluctuations to the order parameter, and thus to the cross-relaxation rate, are given for various proton pairs in antamanide. The points with $S_{\Omega,kl}^2$ below 0.6 belong to pairs that involve at least one of the Phe[6] side-chain protons. All backbone pairs are restricted to $S_{r,kl}^2$, $S_{\Omega,kl} > 0.9$, in agreement with the fluctuations listed in Table I. It is obvious that there is little correlation between the magnitudes of the two order parameters.

(36) Henry, E. R.; Szabo, A. *J. Chem. Phys.* **1985**, *82*, 4753.

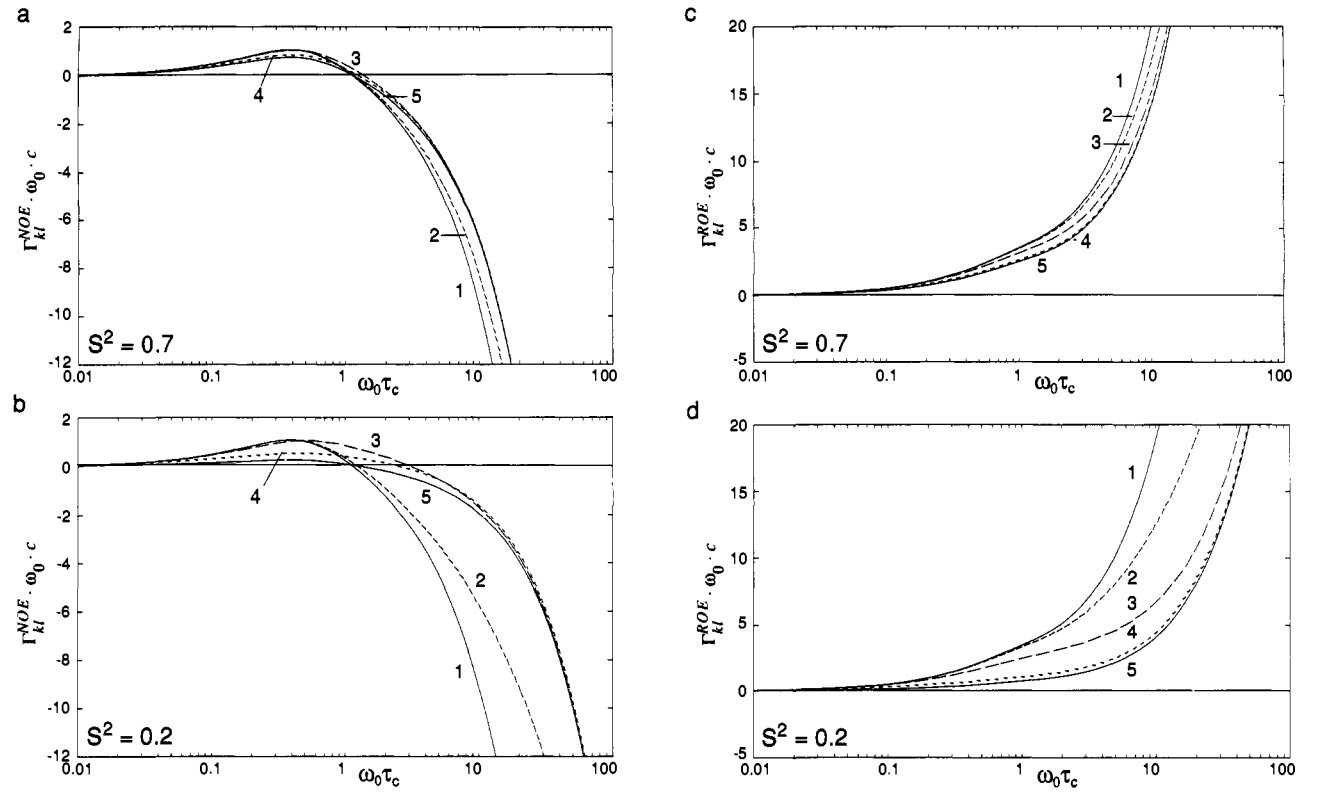

Figure 7. Effect of variable $\tau_c\omega_0$, $\tau_{kl}\omega_0$, and S_{kl}^2 on $\Gamma_{kl}^{NOE,dyn}$ and $\Gamma_{kl}^{ROE,dyn}$. Five curves are shown for $\tau_{kl}\omega_0$ = 100 (1), 10 (2), 1 (3), 10^{-1} (4), and 10^{-2} (5) as a function of $\tau_c\omega_0$. Parts a and b refer to the quantities $\Gamma_{kl}^{NOE}\omega_0 c$ while parts c and d show the behavior of $\Gamma_{kl}^{ROE}\omega_0 c$ where $c = \langle 1/r^6\rangle^{-1}q^{-1}$ for S^2 = 0.7 and 0.2, respectively. Γ_{kl}^{NOE} and Γ_{kl}^{ROE} are defined in eqs 16 and 17.

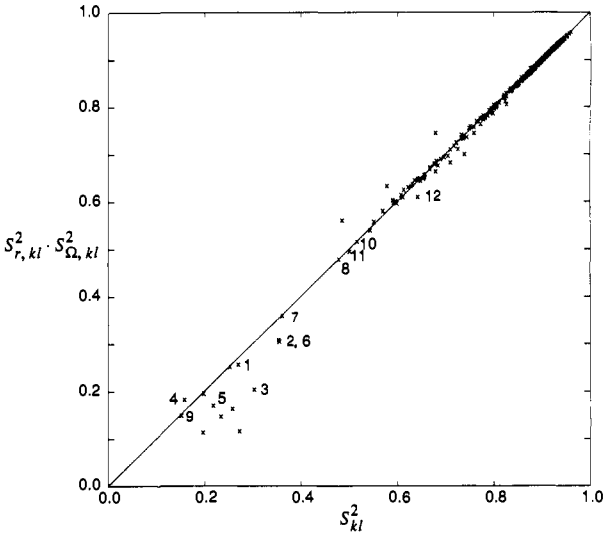

Figure 8. $S_{r,kl}^2 S_{\Omega,kl}^2$ plotted versus S_{kl}^2 to check the product approximation of eq 20 for the proton pairs in antamanide with average distances smaller than 4.5 Å.

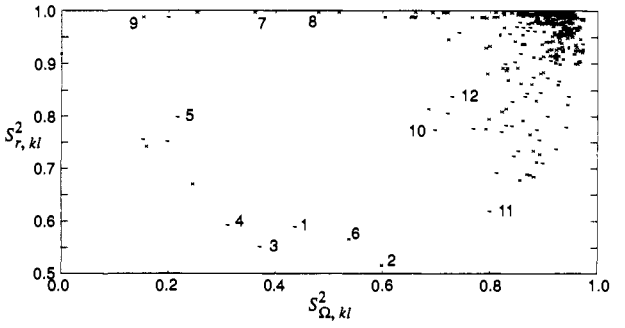

Figure 9. Correlation plot of angular and radial order parameters $S_{\Omega,kl}^2$ and $S_{r,kl}^2$ for the proton pairs used in Figure 8.

The numerical values of the order parameters $S_{\Omega,kl}^2$ and $S_{r,kl}^2$ obtained in the present analysis are upper limits, since not all aspects of proton motion are well represented. First, proton bond stretching is suppressed by using SHAKE to allow an integration time step of 1 fs (cf. section 3). This is expected to be a small effect. Second, there is the limited time range of the simulation which leads to an underestimate of slow large scale motion (e.g. ring flips).

A qualitative relation between the radial fluctuation $\sigma(r_{kl}) = \langle(r_{kl} - \langle r_{kl}\rangle)^2\rangle^{1/2}$ and the radial order parameter $S_{r,kl}^2$ is expected since large amplitude fluctuations contribute to a reduced order parameter and vice versa. Figure 10a shows that there indeed is a qualitative correlation of the two quantities. The exact relation seems to depend on the nature of the motions involved. To clarify the dependence, we show in Figure 9a the results from three model calculations. The nearly straight solid line corresponds to a Gaussian distribution of the fluctuation amplitudes

$$p(r_{kl}) = \frac{1}{\sigma(r_{kl})\sqrt{2\pi}} \exp[-(r_{kl} - r_{kl0})^2/(2\sigma(r_{kl})^2)] \quad (24)$$

with a cutoff at a 5% amplitude level. The dash–dotted line corresponds to a uniform distance distribution (square well) within an interval Δr corresponding to $\sigma(r_{kl}) = \Delta r/\sqrt{12}$. The dashed line refers to a two-site jump model with equal populations in the two sites. For small fluctuations, all three models agree well with the MD data. For larger fluctuations, the data become more sensitive to the distribution function. For example, the order parameter S_r^2 for the two-site jump model is always larger than 0.5. The good fit obtained with the Gaussian model for $S_{r,kl}^2 \geq 0.7$ is not surprising since the distributions in r_{kl} are in fact nearly Gaussian in many cases (see Figure 4). Points in the lower right corner correspond to pairs involving the aromatic protons of Phe^6. These values can be interpreted as arising from two-site exchange between harmonic wells with a Gaussian local fluctuation distribution. For the pair Phe^{6}NH-Phe^{6}H$_{\delta 2}$ {3}, this behavior is shown in Figure 4c.

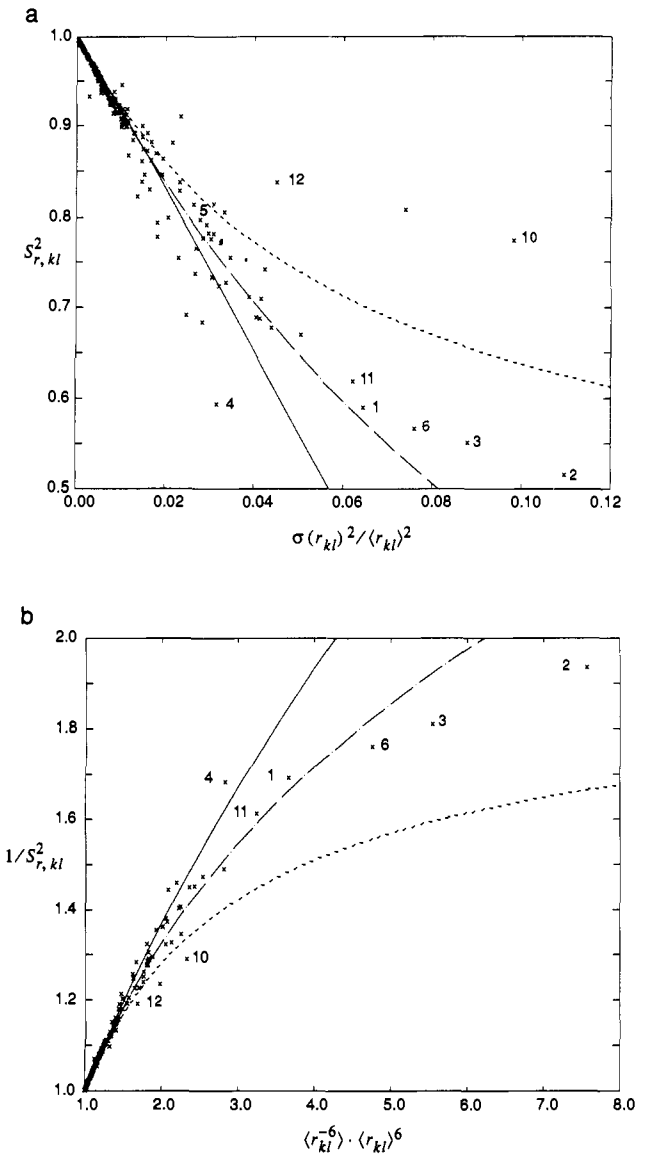

Figure 10. (a) Correlation of relative radial fluctuation $(\sigma(r_{kl})/\langle r_{kl}\rangle)^2$ and radial order parameter $S^2_{r,kl}$. The crosses represent the results of the MD simulation of antamanide. The solid line corresponds to a Gaussian radial distribution, the dash-dotted line to a square well distribution, and the dashed line to an equipopulated two-site distribution. For radial order parameters close to 1, all three distributions can be approximated by the linear relation $S^2_{r,kl} = 1-8.14\ (\sigma(r_{kl})/\langle r_{kl}\rangle)^2$. (b) Quantification of inequality eq 22 $\langle 1/r_{kl}^6\rangle \geq \langle 1/r_{kl}^3\rangle^2 \geq 1/\langle r_{kl}\rangle^6$ by plotting $1/S^2_{r,kl}$ vs $\langle 1/r_{kl}^6\rangle\langle r_{kl}\rangle^6$. The curves correspond to the same models as shown in part a.

The points in the upper right of Figure 10a can be traced back to unequally populated multiple site systems. For example, the pair $Pro^8H_{\delta 1}$–$Phe^9H_{\epsilon 1}$ {10} exhibits a double peaked distribution with the dominant maximum centered at 2.7 Å and a second much smaller maximum at 7.0 Å (see Figure 4e,f). The second maximum influences the variance $\sigma(r_{kl})$ but has virtually no effect on the order parameter $S^2_{r,kl}$ which is dominated by the distribution near the smaller value of $r = 2.7$ Å. This is a consequence of the strongly nonlinear averaging of $\langle 1/r_{kl}^3\rangle^2$ and $\langle 1/r_{kl}^6\rangle$ that determine $S^2_{r,kl}$.

Figure 10b shows a graphical presentation of the inequalities of eq 23 applied to the MD data and to the three analytical distance distributions used in Figure 9a. Radial order parameters above 0.85, corresponding to $1/S_r^2 < 1.18$, show excellent agreement with all three distribution models, which are very similar in this range. For smaller S_r^2 the results are more dependent on the details of the distance distribution. Under favorable circumstances this graph can be used to estimate S_r^2 from experimental data (see section 6).

4.4. Order Parameters for Simple Analytical Models. We compute in this section the radial, angular, and total order parameters for four motional model systems that involve discrete jumps between two or three equally populated sites in order to check the validity of the product approximation of eq 20.

The models discussed in the following are limiting cases that are not directly comparable to situations in antamanide but nevertheless illustrate the range of validity of the product approximation.

(i) General Expressions. We assume a general discrete lattice jump model where a proton pair has N different possible sites, each characterized by an internuclear vector $\mathbf{r}_i$, measured in a molecule fixed frame, and by its probability p_i, $i = 1, ..., N$.

The order parameter can be calculated from eq 7

$$S^2 = \langle 1/r^6\rangle^{-1} \lim_{t\to\infty} \left\langle \frac{P_2(\cos\chi(t))}{r^3(t_0+t)r^3(t_0)} \right\rangle = [\sum_{i=1}^{N} p_i r_i^{-6}]^{-1} \lim_{t\to\infty} \sum_{i,j=1}^{N} p_i P(i,t_0|j,t_0+t) \frac{P_2(\cos\chi_{ij})}{r_i^3 r_j^3} \quad (25)$$

where $P(i,t_0|j,t)$ is the conditional probability for the proton pair to be at site j at time t, if it was at site i at time t_0, and $\cos\chi_{ij} = \mathbf{r}_i\cdot\mathbf{r}_j/|\mathbf{r}_i||\mathbf{r}_j|$. Since $\lim_{t\to\infty} P(i,t_0|j,t_0+t) = p_j$ for a stationary stochastic process, we have

$$S^2 = [\sum_{i=1}^{N} p_i r_i^{-6}]^{-1} \sum_{i,j=1}^{N} p_i p_j \frac{P_2(\cos\chi_{ij})}{r_i^3 r_j^3} \quad (26)$$

Analogously, S^2_Ω and S^2_r are calculated according to

$$S^2_\Omega = \sum_{i,j=1}^{N} p_i p_j P_2(\cos\chi_{ij}) \quad (27)$$

and

$$S^2_r = [\sum_{i=1}^{N} p_i r_i^{-6}]^{-1} \left[\sum_{j=1}^{N} p_j r_j^{-3}\right]^2 \quad (28)$$

(ii) Three-Site Model with Equal Populations. We assume a molecular fragment corresponding to the $C^\alpha H$–$C^\beta H$ part of an amino acid residue and suppose that the $C^\beta H$ fragment can assume three equally populated rotational positions in trans and gauche relations to $C^\alpha H$. Assuming tetrahedral bond angles and $r_{CC} = 1.54$ Å, $r_{CH} = 1.09$ Å, one finds based on eqs 26–28 the following order parameters for the H_α–H_β vector

$$S^2_r = 0.937 \qquad S^2_\Omega = 0.624$$

and

$$S^2_r S^2_\Omega = 0.584 \qquad S^2 = 0.582$$

The product rule is well satisfied in this case.

(iii) Two-Site Model with Equal Populations. The model again refers to a $C^\alpha H$–$C^\beta H$ fragment. In this case we assume, however, that one of the two gauche rotamers remains unpopulated. This leads to the order parameters

$$S^2_r = 0.916 \qquad S^2_\Omega = 0.745$$

and

$$S^2_r S^2_\Omega = 0.683 \qquad S^2 = 0.704$$

The deviation between the product and S^2 is slightly larger in this case and correlation effects are noticeable. Nevertheless, the product approximation remains useful.

(iv) General Two-Site Jump Model. We assume an internuclear vector $\mathbf{r}$ that can jump between two energetically equivalent positions $\mathbf{r}_1$ and $\mathbf{r}_2$. The jump corresponds to a radial change $2\sigma = ||\mathbf{r}_1| - |\mathbf{r}_2||$ and a rotation by an angle χ with $\cos\chi = (\mathbf{r}_1\cdot\mathbf{r}_2)/|\mathbf{r}_1||\mathbf{r}_2|$. The product of the order parameters $S^2_r S^2_\Omega$ and the integral order parameter S^2 have been computed for pairs σ and χ. The resulting plots are shown in Figure 11. A comparison of the plots demonstrates that the order parameter S^2, defined in eq 10, is rather insensitive to correlations of the radial and angular fluc-

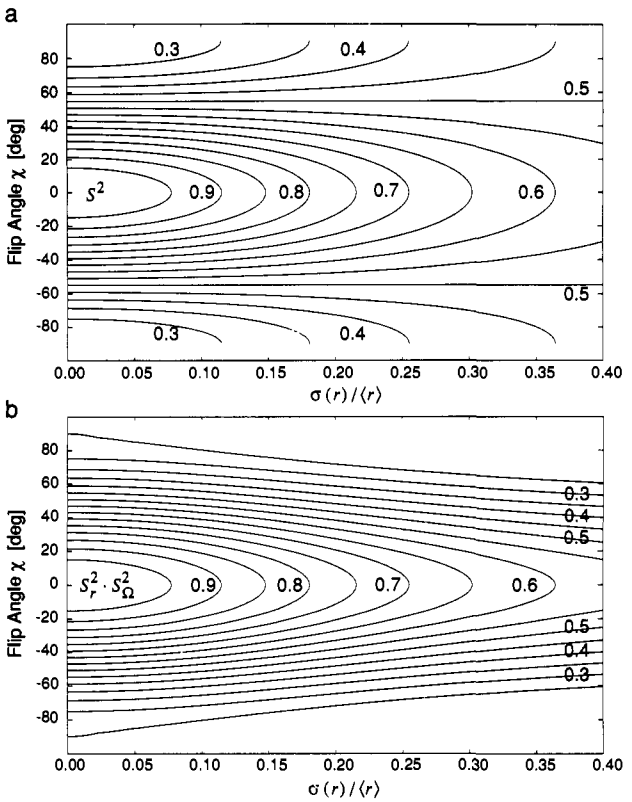

Figure 11. Application of product approximation for the two-site lattice jump model. Computed values for (a) S^2 and (b) $S_r^2 S_\Omega^2$ are presented in contour plots as functions of the flip angle χ and distance fluctuation $2\sigma = |r_1 - r_2|$.

tuations as long as $S^2 > 0.6$. For this case, the deviations between $S_r^2 S_\Omega^2$ and S^2 are smaller than 0.1. For small order parameters S^2, the deviations become more significant. Normally, there are several motional modes that affect the same internuclear vector and correlation effects are smaller than for the extreme single jump process, where distance and angle are altered at the same time, as assumed here. This can be seen from the good agreement obtained over a wide range of S^2 values for antamanide in Figure 8. It should also be noted that for large angular flips χ, the concept of order parameters becomes less meaningful because of the nonlinearity and periodicity of $P_2(\cos\chi)$. For instance, $\chi = 180°$ may induce a large conformational change, but it does not affect the angular order parameter and the cross-relaxation rate constant.

(v) Double Sphere Diffusion. In the diffusion model to be discussed here, both protons involved in the cross-relaxation process are allowed to diffuse freely and independently within spheres of radius r with center separation d. Figure 12 shows the dependence of S^2, S_Ω^2, S_r^2, and $S_\Omega^2 S_r^2$ for this model as a function of $2r/d$. For each point in the plot, 10000 different internuclear vectors were constructed from random pairs of vectors $\mathbf{r}_1$ and $\mathbf{r}_2$ between the two spheres. The figure demonstrates that the product approximation is well fulfilled. The slightly irregular form of the curves is due to the limited number of sampling points (100 points per sphere). A particular feature of this model is that the radial order parameter is systematically smaller than the angular order parameter ($S_r^2 < S_\Omega^2$). This contrasts with the results of molecular dynamics simulation for the majority of the proton pairs in antamanide (see Figure 9) and suggests that in the simulations there is correlation in the atomic motion that restrains the variation in interparticle distances. Protein simulations have shown this to be true for nuclei that are separated by distances of the range considered here.[34]

5. Cross-Relaxation Rates in Antamanide

In this section we consider the influence of intramolecular motion on the measurement of average internuclear distances in molecules through cross-relaxation rates, using antamanide as an

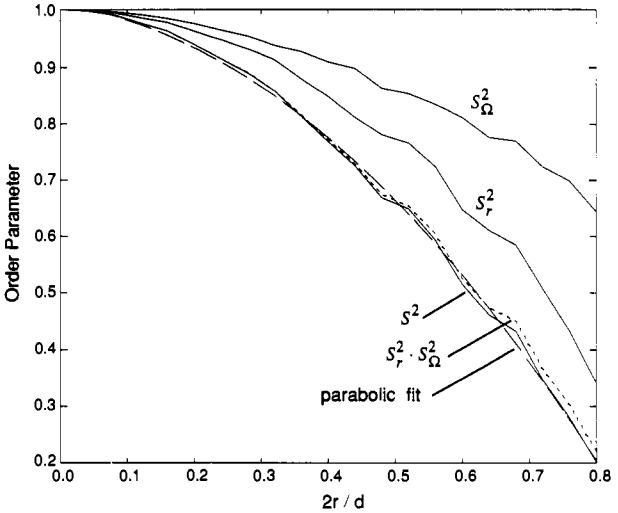

Figure 12. Order parameters for double sphere diffusion as functions of the ratio of the diameter $2r$ to distance d of two equal spheres. The approximation of the function $S^2(2r/d)$ by the relation $S^2 \cong 1.01 - 0.16(2r/d) - 1.06(2r/d)^2$, obtained by fitting the data, is also shown.

example. For a rigid and isotropically rotating molecule, the cross-relaxation rate constant from NOESY or ROESY spectra can be interpreted quantitatively by a calibration of the experimental rate constants with spin pairs of known distance. Often geminal proton pairs are used for this purpose. The internuclear distance is then proportional to the ratio of the sixth root of the inverse cross-relaxation rates

$$r_{kl} = [\Gamma_{geminal}/\Gamma_{kl}]^{1/6} r_{geminal} \qquad (29)$$

Deviations from eq 29 are expected in the presence of intramolecular motion, as has been discussed in a previous molecular dynamics analysis of this problem.[12] Figure 13 correlates the sixth root of the inverse cross-relaxation rate constant for various proton pairs calculated from the spectral densities obtained from the antamanide trajectory with the linearly averaged internuclear distance from the same trajectory. In Figure 13a the NOESY cross-relaxation rate constants, computed from eq 2a, are plotted; in Figure 13b, the ROESY cross-relaxation rate constants from eq 2b are shown. The straight line, corresponding to eq 29, connects the origin with the points for the geminal protons in the molecule. It is seen that for most proton pairs the NOESY and ROESY cross-relaxation rates lead to an underestimation of the distance with deviations up to 0.3 Å for the NOESY [$Pro^8H_{\delta 1}$–Phe^9H_ζ{11}] and 1.0 Å for ROESY [$Phe^5H_{\beta 2}$–$Phe^6H_{\delta 2}${2}]. The origin is found in the fact, mentioned in section 4, that the geminal proton pairs experience predominantly angular fluctuations which reduce the cross-relaxation rate (the distance fluctuations are negligible), so that the rates for other proton pairs appear to be correspondingly larger. It is possible to correct for this effect by scaling the slope of the calibration line. A numerical fit yields a scaling factor of 1.016 for both NOE-derived (Figure 13a) and ROE-derived distances (Figure 13b) (of proton pairs not involved in side-chain transitions) with which the measured distances have to be multiplied. It is not unlikely that molecules of comparable flexibility (e.g. other cyclic peptides) behave similarly so that the same scaling of distances might be applicable.

There are also cross peaks significantly above the straight lines in Figure 13. They belong to proton pairs with very high angular mobility and strongly averaged dipolar interaction. This occurs in particular for cross peaks associated with the protons of the mobile phenyl ring of Phe^6, e.g. $Phe^6H_{\epsilon 1}$–$Phe^6H_{\epsilon 2}${8}. So. e NOE cross peaks even change their sign as a consequence of strong and relatively slow internal fluctuations. These proton pairs are indicated in Figure 13a in the lower graph. For these pairs, $-(\Gamma_{kl}^{NOE,dyn})^{-16}$ is plotted as a function of $\langle r_{kl}\rangle$. They all represent intraresidue proton pairs of Phe^6, such as $Phe^6H_{\beta 1}$–$Phe^6H_{\delta 1}$ {5} and $Phe^6H_{\epsilon 2}$–Phe^6H_ζ {9}. The sign change occurs due to a differential scaling of the terms $J_{kl}(0)$ and $J_{kl}(2\omega_0)$ in eq 2a by the

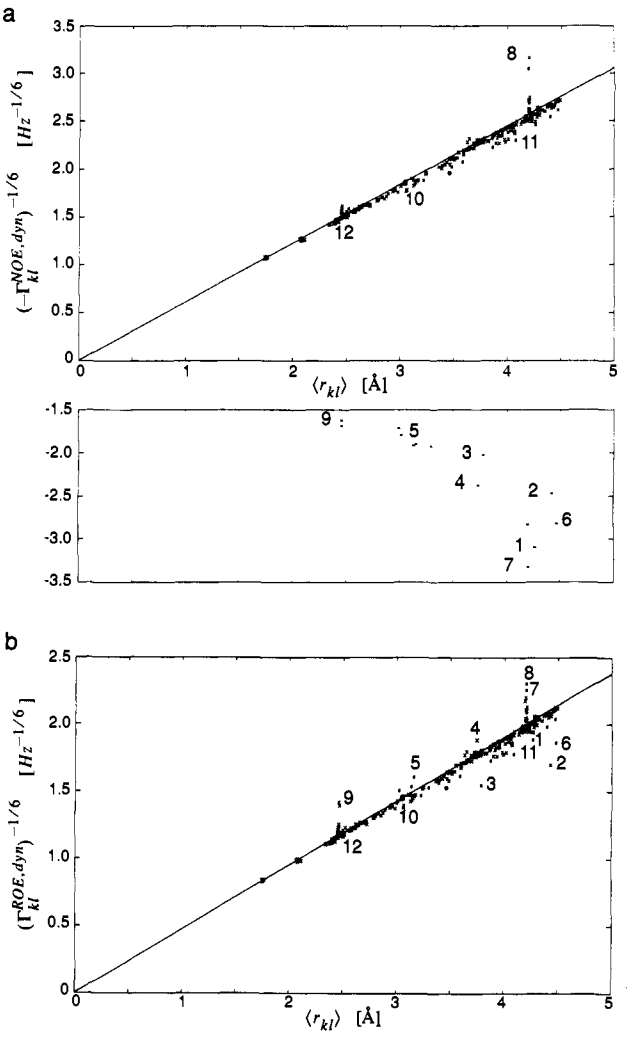

Figure 13. Correlation of cross-relaxation rate constants and average distance for all proton pairs in antamanide with an average distance smaller than 4.5 Å. The straight lines correspond to the calibration curves based on the cross relaxation of geminal protons. These lines are often used in the evaluation of (a) NOESY distances and (b) ROESY distances. In part a, the proton pairs with positive $\Gamma_{kl}^{NOE,dyn}$, due to strong internal motion, are shown in the lower frame where $-[\Gamma_{kl}^{NOE,dyn}]^{-1/6}$ is plotted vs the average distance.

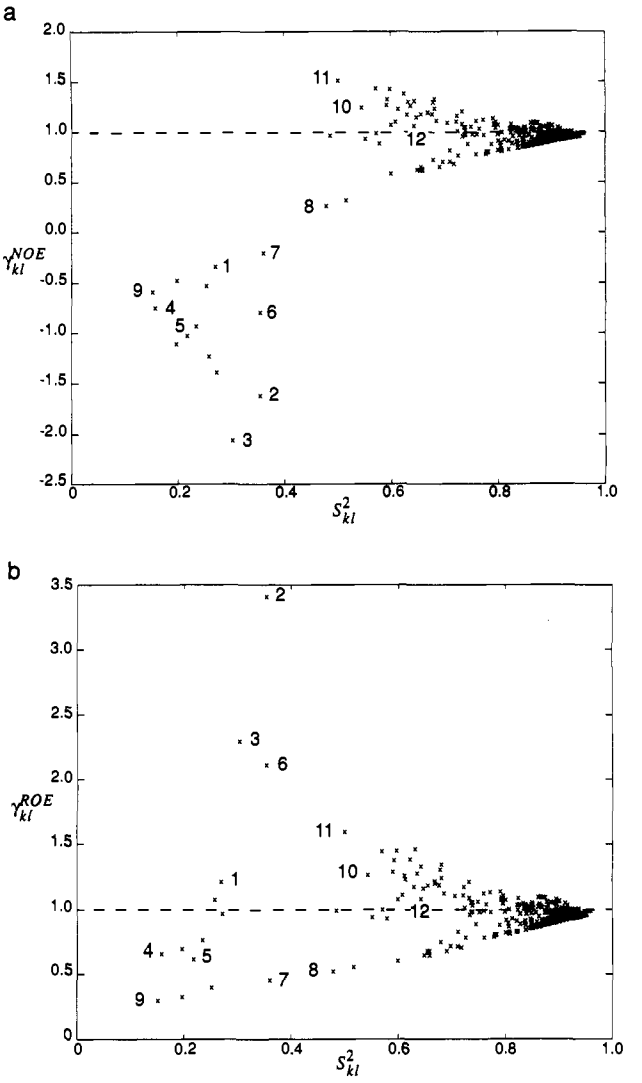

Figure 14. Correlation (a) between the relative cross-relaxation rate constant $\gamma_{kl}^{NOE} = \Gamma_{kl}^{NOE,dyn}/\Gamma_{kl}^{NOE,stat}$ and S_{kl}^2 and (b) between $\gamma_{kl}^{ROE} = \Gamma_{kl}^{ROE,dyn}/\Gamma_{kl}^{ROE,stat}$ and S_{kl}^2 of the proton pairs displayed in Figure 13.

intramolecular dynamics (see eqs 17 and 18). In the corresponding ROESY spectrum (Figure 13b) a sign change of the cross-peak intensities cannot occur (cf. eq 2b). By use of geminal protons for distance calibration in ROESY, an underestimation of internuclear distances occurs more often than for NOESY. This feature reflects a delicate competition between the second term in eq 17 and S_r^2. In the case of NOESY, the second term has a stronger influence which results in a decrease of the cross-relaxation rate. In the case of ROESY, the effect of S_r^2 dominates and the second term in eq 17 is of minor importance. Qualitative differences in the behavior of a proton pair in NOESY and in ROESY can unambiguously be attributed to the presence of medium fast motional processes.

To analyze the influence of the order parameters on the accuracy of distances determined from cross-relaxation rates, it is convenient to introduce the relative cross-relaxation rate constants $\gamma_{NOE,kl} = \Gamma_{NOE,kl}^{dyn}/\Gamma_{NOE,kl}^{stat}$ and $\gamma_{ROE,kl} = \Gamma_{ROE,kl}^{dyn}/\Gamma_{ROE,kl}^{stat}$ where $\Gamma_{NOE,kl}^{stat}$ and $\Gamma_{ROE,kl}^{stat}$ are computed based on average internuclear distances $\langle r_{kl} \rangle$ extracted from the trajectory, and using eqs 19, 2a, and 2b, with the assumption that the molecule is rigid, while $\Gamma_{NOE,kl}^{dyn}$ and $\Gamma_{ROE,kl}^{dyn}$ are obtained from eqs 2–7, using the molecular dynamics trajectory.

Parts a and b of Figure 14 correlate $\gamma_{NOE,kl}$ and $\gamma_{ROE,kl}$, respectively, with the total order parameter S_{kl}^2. Although S_{kl}^2 reflects the degree of intramolecular motion and larger deviations of γ_{kl} from 1 are associated with smaller S_{kl}^2, it is not a good measure of the influence of motion on cross relaxation. In particular, the relative cross-relaxation rate constant γ_{kl} can be larger or smaller than 1, irrespective of S_{kl}^2. This is true for both NOE and ROE cross-relaxation rates.

The lack of correlation seen in Figure 14 is caused by the opposite effects of radial and angular motion. It is therefore of advantage to separate the radial and angular contributions. One may try to correlate the γ_{kl} with the ratio $S_{\Omega,kl}^2/S_{r,kl}^2$. Figure 15 shows that for $S_{\Omega,kl}^2/S_{r,kl}^2 < 1$ the ratio γ_{kl} is predominantly smaller than 1, while for $S_{\Omega,kl}^2/S_{r,kl}^2 > 1$, the ratio γ_{kl} is mostly larger than 1. In the range 0.5–1.2 for NOESY and 0.2–1.3 for ROESY, there is nearly linear relation for a majority of proton pairs. However, some proton pairs with large deviations are apparent. There are again proton pairs that exhibit strong deviations of opposite sign for NOE and ROE cross relaxation, such as the pairs $Phe^5H_{\beta 2}$–$Phe^6H_{\delta 2}$ {2} and Phe^6NH–$Phe^6H_{\delta 2}$ {3}. Nevertheless the general correlation is apparent in contrast to the missing correlation with S_{kl}^2 in Figure 14.

6. Analysis of Intramolecular Motion via Cross-Relaxation Measurements

Since there is a significant influence of intramolecular motion on cross-relaxation rates, their measurement can provide information on intramolecular motion. If only a single measurement is available, it is not possible to separate the various factors, such as the internuclear separation $\langle r_{kl} \rangle$, the order parameters S_{kl}^2, $S_{\Omega,kl}^2$, and $S_{r,kl}^2$, and the correlation time τ_{kl}. However, in principle, the

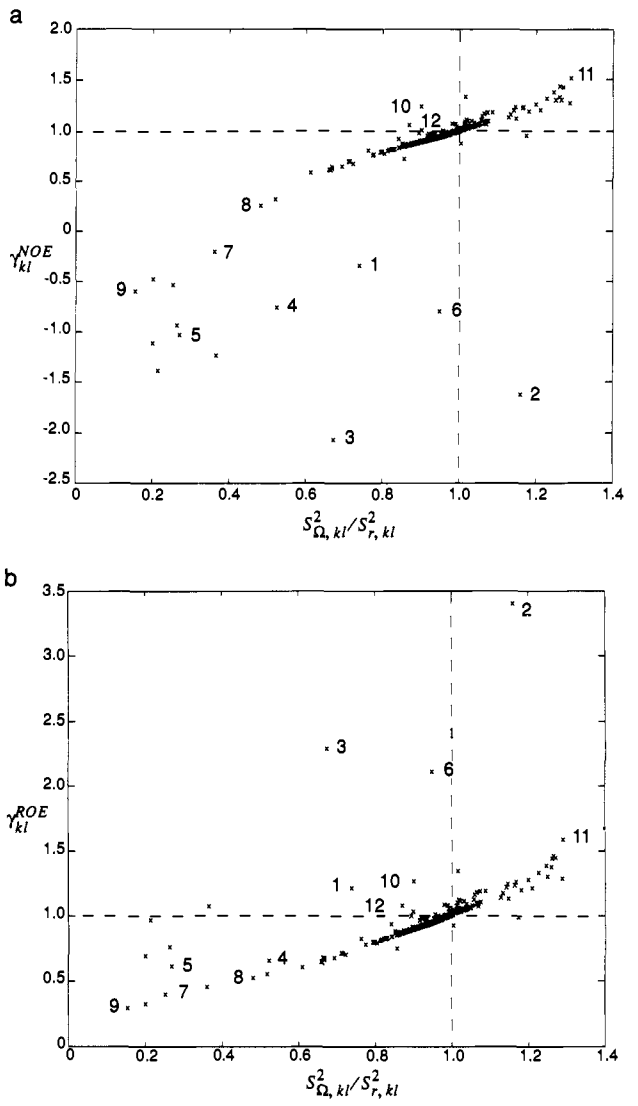

Figure 15. Correlation (a) between the relative cross-relaxation rate constant γ_{kl}^{NOE} and $S^2_{\Omega,kl}/S^2_{r,kl}$ and (b) between γ_{kl}^{ROE} and $S^2_{\Omega,kl}/S^2_{r,kl}$ of the proton pairs displayed in Figure 13.

NOE and ROE cross-relaxation rate constants Γ_{kl}^{NOE} and Γ_{kl}^{ROE} can be measured as functions of the magnetic field strength B_0 and provide information that may allow a separation of the various factors. In addition, the overall tumbling correlation time could be varied by changing the viscosity of the solvent to displace the time-scale window for the observation of intramolecular motion. In this section, we examine the feasibility of using such information by means of model calculations.

The spin–lattice and rotating-frame relaxation times $T_{1,k}$ and $T_{1\rho,k}$ of a spin k can be quite sensitive to intramolecular motion. However because $T_{1,k}$ and $T_{1\rho,k}$ refer to a single spin, the contributions from interactions with different neighboring spins and of different relaxation mechanisms cannot be distinguished readily. This is a severe problem for the interpretation of proton relaxation times. To avoid this difficulty, many studies of protein motion have focused on carbon-13 and nitrogen-15 relaxation times.[37,38] At not too high magnetic fields, where relaxation by chemical shielding anisotropy can be neglected, the dominant relaxation mechanism is the dipolar interaction with the directly bonded proton(s), and relaxation rates can be interpreted unambiguously in terms of the motion of the CH or NH vector(s). The relevant heteronuclear dipolar interactions are one-bond interactions that are sensitive only to local intramolecular dynamics. At high magnetic fields, relaxation by chemical shielding anisotropy becomes nonnegligible and makes the interpretation more difficult.

The use of homonuclear cross relaxation or protons for dynamics studies might be attractive for two reasons: (a) the cross-relaxation rate monitors exclusively a single-pair interaction irrespective of the complexity of the interaction network; (b) long-range NOE's and ROE's are a potential source of information concerning dynamical processes of a more collective nature, for example fast segmental motions, which have hitherto been inaccessible by NMR relaxation measurements. Thus, such proton studies may be useful to examine a wide range of behavior.

To obtain a measure for intramolecular motion that is independent of the magnetic nuclear dipolar interaction strength, a ratio between two measured rates can be used. In the present case, it is convenient to compare measurements in the laboratory and rotating frame. The ratio

$$\rho_{kl} = \Gamma_{kl}^{NOE}/\Gamma_{kl}^{ROE} \tag{30}$$

calculated from eqs 2a, 2b, and 12 is plotted in Figure 16 for two correlation times τ_c, two order parameters S^2_{kl}, and ten ratios τ_{kl}/τ_c as a function of the resonance frequency $\omega_0/2\pi$. It should be noted that ρ_{kl} is independent of the quantity S^2_{fast} introduced in eq 11. The case $\tau_c = 0.6$ ns represents a small biomolecule (e.g. a peptide, such as antamanide) while the case $\tau_c = 6$ ns corresponds to a medium size protein. The four graphs show that rapid internal motion leads toward curve 10 in Figure 16 that is asymptotically independent of the internal correlation time τ_{kl} and depends exclusively on $\omega_0\tau_c$. Figure 16 demonstrates that ρ_{kl} has informative behavior if both of the following two conditions are fulfilled

(i) $$0.1 < \tau_{kl}/\tau_c < 10$$

(ii) $$0.1 < \omega_0\tau_{kl}^{tot} < 10$$

Inequality i is necessary for the relaxation rates to depend on τ_{kl} and inequality ii to guarantee that the NOESY and ROESY rates differ sufficiently due to their different spectral intensity contributions (eq 2). From the previous section it can be concluded that the proton pairs involved in the side chain motion of Phe^6 fulfill both inequalities.

Although the magnetic field dependence is characteristically different for different values of S^2_{kl} and τ_{kl}/τ_c, it might not be easy to apply the method in practice and to obtain accurate enough values for the two quantities due to sensitivity problems. However, careful measurements would allow one to detect and to localize intramolecular motion at least qualitatively and to obtain limits for both S^2_{kl} and for τ_{kl}/τ_c.

If in favorable cases values for S^2_{kl} and τ_{kl} have been determined from such an analysis and additionally the average distance $\langle r_{kl}\rangle$ is available from other sources (e.g. X-ray data), an approximate value for S^2_r can be obtained from the empirical relationship between $1/S^2_r$ and $\langle 1/r^6\rangle\cdot\langle r\rangle^6$ visualized in Figure 10b. By use of the product approach, an estimate for the angular order parameter is given by $S^2_\Omega \simeq S^2/S^2_r$. A systematic evaluation of these parameters for different regions of the molecule could be used to improve the understanding of the nature of motion in biopolymers. It would also be of interest to combine such NMR results with motional information from X-ray diffraction and incoherent neutron or light scattering to test the consistency of the interpretation of the various experiments.

7. Conclusions

In this paper we have extended the time scale and analysis of molecular dynamics simulations to determine the influence of rapid intramolecular motional processes on nuclear relaxation. An 800-ps molecular dynamics simulation of the cyclic decapeptide antamanide in chloroform was used for the study. The results demonstrate that most of the effects of the calculated intramolecular motion on relaxation behavior can be described by using a product approximation which separates radial and angular order parameters and an effective internal correlation time. Such a simple description summarizes the information of intramolecular mobility obtainable from NMR in the time range considered. Comparisons with analytic models indicate under what conditions

(37) Nirmala, N. R.; Wagner, G. *J. Am. Chem. Soc.* **1988**, *110*, 7557.
(38) Clore, G. M.; Driscoll, P. C.; Wingfield, P. T.; Gronenborn, A. M. *Biochemistry* **1990**, *29*, 7387.

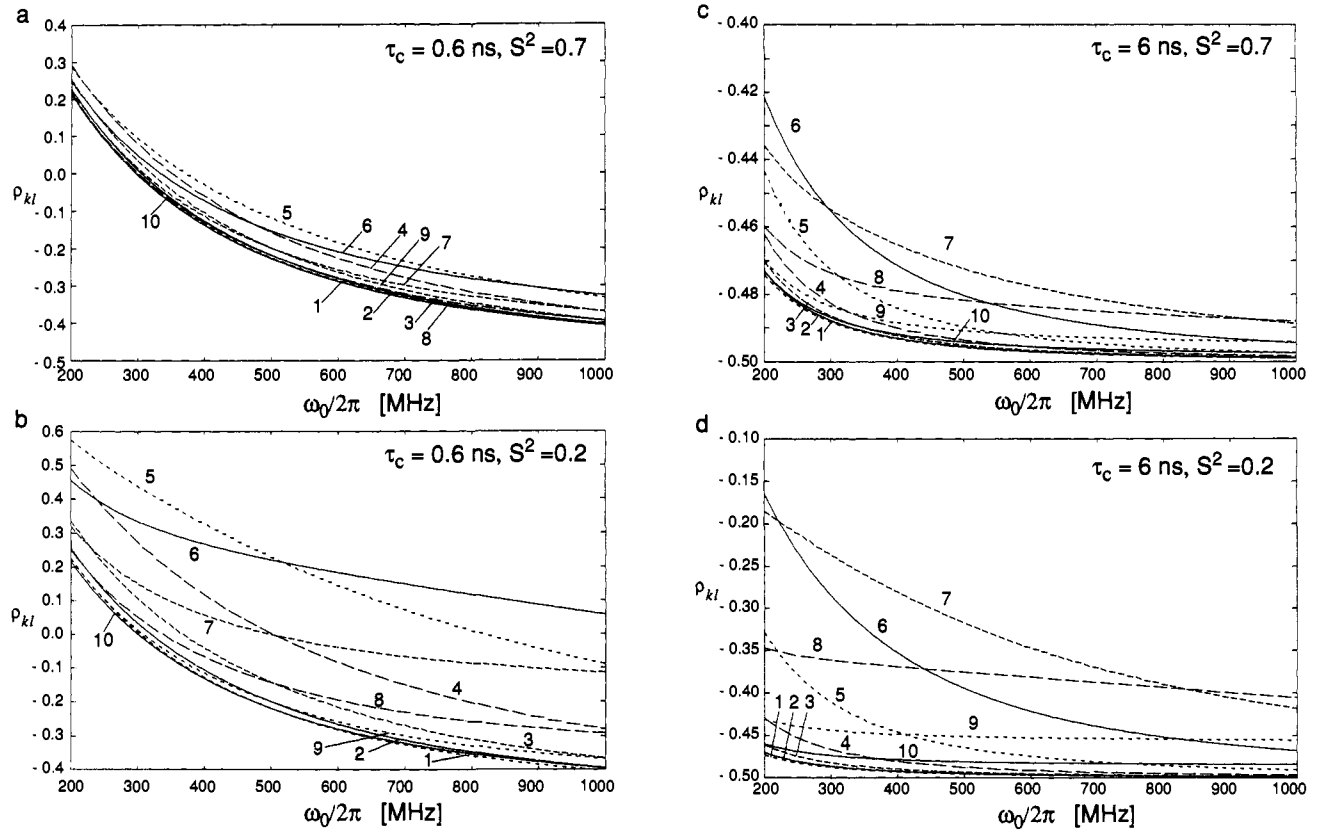

Figure 16. Influence of variable parameters ω_0, τ_c, τ_{kl}/τ_c, and S^2_{kl} on $\rho_{kl} = \Gamma^{NOE,dyn}_{kl}/\Gamma^{ROE,dyn}_{kl}$ using eq 13b. In each plot (a–d) 10 curves are shown for $\tau_{kl}/\tau_c = 3.16 \times 10^{1}$ (1), 10 (2), 3.16 (3), 1 (4), 3.16×10^{-1} (5), 10^{-1} (6), 3.16×10^{-2} (7), 10^{-2} (8), 3.16×10^{-3} (9), 10^{-3} (10). Along the abscissa ω_0 is varied. The parameters S^2_{kl} and τ_c chosen were as follows: (a) S^2_{kl} = 0.7, τ_c = 0.6 ns; (b) S^2_{kl} = 0.2, τ_c = 0.6 ns; (c) S^2_{kl} = 0.7, τ_c = 6.0 ns; (d) S^2_{kl} = 0.2, τ_c = 6.0 ns.

the product approximation is satisfied, although the simplifying assumptions of the models about the internal motions are not fully realistic. A procedure has been proposed to extract motional parameters from a combination of NOESY and ROESY experiments in cases where intramolecular motion can be characterized by correlation functions with a monoexponential decay.

A limitation of this study, as well as earlier work based on shorter simulations, is that the simulations are not long enough to include the full range of motions of importance to NMR relaxation. Extensions are conceivable in several directions, some of which require substantially increased computer power. (i) To cover the slower motional processes by direct MD trajectories would require an increase in the length of the simulations by several orders of magnitude; this is feasible in principle but expensive at this time. Alternatively, special methods (e.g. potentials of mean force) might be used to overcome the time scale problem for specific groups. (ii) In order to study the effects of other biomolecular motional features, not displayed by cyclic peptides of the size of antamanide, similar studies of medium-size proteins would be attractive; some work of this type is being done by C. B. Post (private communication) based on a simulation of lysozyme. (iii) Some of the results could also be influenced by the chosen initial molecular structure and the choice of potential. Averaging over an ensemble of MD trajectories for different initial structures would be of interest, as would be the use of the new all-hydrogen potential that has been developed at Harvard. As a part of such a larger scale simulation effort, it is important that also more detailed experimental information is available to adjust the computational model. The most relevant measurements in this context are relaxation studies of various kinds and sophistication that allow to deduce correlation and cross-correlation functions of intramolecular motional processes within the limits mentioned in this paper. Of particular value are measurements that are sensitive to individual pair interactions such as advanced cross-relaxation studies in the context of 2D spectroscopy. By a joint program of improved simulations and extensive experiments, it should be possible to obtain a more detailed picture of the internal motions in biologically relevant molecules that might be of importance for their function.

Acknowledgment. This work was started during a 3-month visit of R.B. at the Department of Chemistry of Harvard University in 1989 and continued during a 3-month visit of B.R. at the Laboratorium für Physikalische Chemie ETH-Zürich. We thank J. Gao and W. L. Jorgensen for providing starting coordinates for a box of chloroform equilibrated at room temperature. The research has been supported in parts by the Swiss and the United States National Science Foundation. The manuscript was processed by Mrs. I. Müller.

Registry No. Antamanide, 16898-32-1.